Volume 13
Number 36
28 September 2021
Pages 15103-15484

Nanoscale

rsc.li/nanoscale

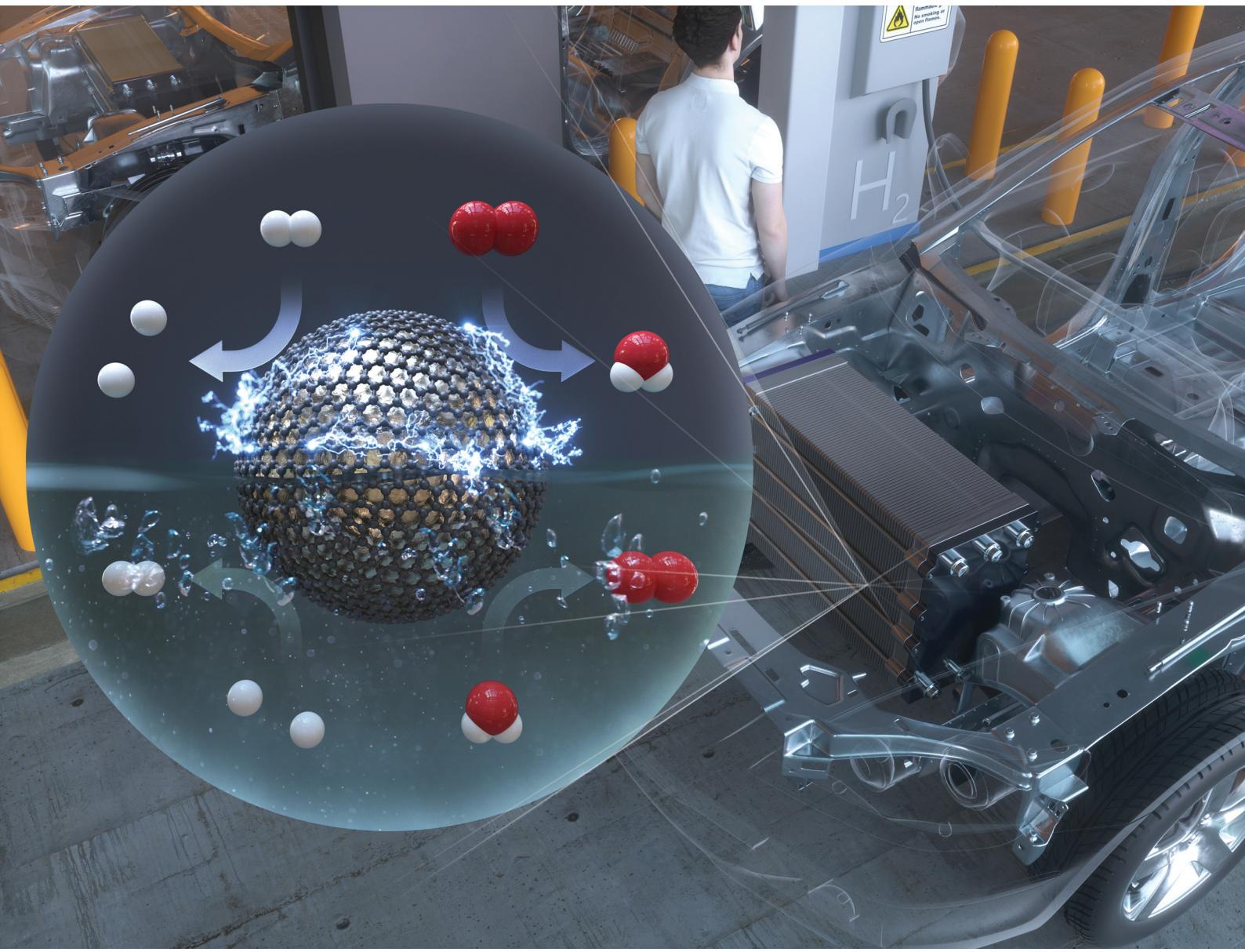

ISSN 2040-3372

ROYAL SOCIETY OF CHEMISTRY

REVIEW ARTICLE
Namgee Jung, Sung Jong Yoo *et al.*
Emerging carbon shell-encapsulated metal nanocatalysts for fuel cells and water electrolysis

NCNST

Nanoscale

REVIEW

View Article Online
View Journal | View Issue

Check for updates

Cite this: *Nanoscale*, 2021, **13**, 15116

Emerging carbon shell-encapsulated metal nanocatalysts for fuel cells and water electrolysis

Jue-Hyuk Jang,†[a] A. Anto Jeffery,†[b] Jiho Min,[b] Namgee Jung *[b] and Sung Jong Yoo *[a,c,d]

Received 1st March 2021,
Accepted 15th July 2021

DOI: 10.1039/d1nr01328a

rsc.li/nanoscale

The development of low-cost, high-efficiency electrocatalysts is of primary importance for hydrogen energy technology. Noble metal-based catalysts have been extensively studied for decades; however, activity and durability issues still remain a challenge. In recent years, carbon shell-encapsulated metal (M@C) catalysts have drawn great attention as novel materials for water electrolysis and fuel cell applications. These electrochemical reactions are governed mainly by interfacial charge transfer between the core metal and the outer carbon shell, which alters the electronic structure of the catalyst surface. Furthermore, the rationally designed and fine-tuned carbon shell plays a very interesting role as a protective layer or molecular sieve layer to improve the performance and durability of energy conversion systems. Herein, we review recent advances in the use of M@C type nanocatalysts for extensive applications in fuel cells and water electrolysis with a focus on the structural design and electronic structure modulation of carbon shell-encapsulated metal/alloys. Finally, we highlight the current challenges and future perspectives of these catalytic materials and related technologies in this field.

Published on 19 2564. Downloaded on 1/2/2569 7:34:44.

1. Introduction

Over the past decades, combustion-based energy technologies have continued to raise serious global concerns, having a significant impact on environmental pollution and climate change caused by tremendous fossil fuel consumption.[1–4] Nevertheless, the global demand for energy is exponentially increasing for a better human life. To simultaneously solve the climate change issues and energy crisis, fuel cells have been intensively developed as one of the promising energy conversion devices. Fuel cells provide clean and efficient ways to convert chemical energy into electrical energy without causing

[a]*Center for Hydrogen·Fuel Cell Research, Korea Institute of Science and Technology (KIST), Seoul 02792, Republic of Korea*
[b]*Graduate School of Energy Science and Technology (GEST), Chungnam National University, 99 Daehak-ro, Yuseong-gu, Daejeon, 34134, Republic of Korea*
[c]*Division of Energy & Environmental Technology, KIST school, University of Science and Technology (UST), Daejeon 34113, Republic of Korea*
[d]*KHU-KIST Department of Converging Science and Technology, Kyung Hee University, Seoul 02447, Republic of Korea*
†These authors have contributed equally.

Jue-Hyuk Jang

Jue-Hyuk Jang received his PhD degree in Renewable Energy from KU-KIST Green School, Graduate School of Energy and Environment, Korea University in 2020. He has been working as a post-doc researcher at the Center for Hydrogen·Fuel cell Research of the Korea Institute of Science and Technology. His current research interests include nanomaterial-based electrocatalysts and membrane-electrode assemblies (MEAs) for electrochemistry.

A. Anto Jeffery

A. Anto Jeffery received his PhD in chemistry from Bangalore University, India in 2017. He has been working as a postdoctoral associate at the Graduate School of Energy Science and Technology in Chungnam National University, Korea under the supervision of Prof. Namgee Jung, since 2019. His research interests focus on the synthesis of novel electrocatalysts for fuel cells and water electrolysis.

This journal is © The Royal Society of Chemistry 2021

Published on 19 2564. Downloaded on 1/2/2569 7:34:44.

environmental issues, while water electrolysis bridges the gap between fuel cell and energy storage technologies.[5–7] Hydrogen energy conversion technologies based on fuel cells and water electrolysis are getting a lot of attention since they can be widely applied in various industries such as transportation and power generation.[8–11]

In fuel cells, hydrogen gas is oxidized *via* the hydrogen oxidation reaction (HOR) at the anode, and oxygen gas is reduced *via* the oxygen reduction reaction (ORR) at the cathode, producing electricity and water.[12–15] In contrast to this, in water electrolysis using an external power supply, pure hydrogen and oxygen gases can be electrochemically produced from water by hydrogen and oxygen evolution reactions, respectively, without emitting carbonaceous byproducts.[16–18] Therefore, the water electrolysis reaction has the reverse mechanism of the fuel cell reaction.

In the past, hydrogen-based technologies have been used only for special and limited purposes, such as power sources for space shuttles due to their high cost.[19,20] However, in recent years, fuel cell systems have become commercially available for applications in fuel cell vehicles (FCVs), residential power supplies, and power plants.[21–23] Accordingly, the hydrogen production technology for fuel cell operation has been extensively studied.[3,24–26] Despite this, to guarantee the performance of fuel cells and water electrolyzers, it is still necessary to develop a highly efficient and durable electrocatalyst, one of the key materials.

Precious metal-based nanoparticles (NPs) such as Pt and Ir have been commonly used in the electrochemical reactions in fuel cells and water electrolyzers.[27–30] However, along with the high cost problems and the lack of noble metal reserves, the challenging goal of further improving their catalytic activity and durability remains. In addition, the development of non-precious metal-based catalysts has been urged to replace the Pt and Ir-based catalysts. For instance, Pt-based alloys have been studied to enhance the HER/ORR and HER performance.[31–33] In addition, Ir- and Ru-based electrocatalysts have been used to reduce the overpotential for the OER in water electrolysis.[34,35] However, precious metal-based alloy catalysts still suffer from dissolution and detachment of metal NPs during the electrochemical reactions.

Meanwhile, to solve the cost problem of noble metals, 3d transition metal (TM)- and carbon-based electrocatalysts such as metal–nitrogen–carbon (M–N–C) and heteroatom-doped graphene catalysts have been developed.[36–40] Non-precious metal catalysts exhibit improved activity and durability; however, not only do they lack the number of active sites, but they also have non-ideal catalyst structures that are not suitable for practical application in compact electrochemical cells.[41–43] In particular, a highly porous electrode structure is required for diffusion of reactants and products, but graphene-based M–N–C catalysts can be easily stacked on the electrode, thereby forming a high-density electrode structure.[44–46]

In recent years, to overcome the limitations of typical catalyst structures, carbon shell-encapsulated metal (M@C) NPs have been proposed as promising catalysts that can be practically used in electrodes.[47–56] Metal NPs are encapsulated by a thin carbon shell through various carbon coating technologies such as chemical vapor deposition (CVD), the polymer coating method, the solvothermal method, and the high-temperature pyrolytic method. However, in M@C NPs, carbon shells play different roles or provide multi-functionality depending on the purpose. For instance, electrochemically active metal NPs such as Pt can be protected by a carbon shell, showing the high durability of the catalyst. On the other hand, the carbon shell directly acts as an active site due to the electronic structure modulated by the core metal NP. In some cases, M@C NPs exhibit high activity simultaneously against a variety of electrochemical reactions (*e.g.*, HER and OER), demonstrating a bi-functional catalyst. Furthermore, the carbon shell with a finely tuned pore structure can be utilized as a molecular sieve layer with selective H_2/O_2 permeability under shut-down/start-up conditions during fuel cell operation.

In this review, starting with the classification of efficient carbon capsulation strategies, the important effects of the carbon shell on the physicochemical properties of M@C NPs

Jiho Min

Jiho Min received his Bachelor's degree from Hanbat University in 2018 and pursued his Master's degree from Graduate School of Energy Science and Technology, Chungnam National University, Korea in 2020 under the supervision of Prof. Namgee Jung. He is currently pursuing his PhD studies at the Graduate School of Energy Science and Technology in Chungnam National University under the supervision of Prof. Namgee Jung. His main research interests focus on the synthesis/design of novel electrocatalysts for fuel cell applications.

Namgee Jung

Namgee Jung received his Ph.D. degree in the Department of Chemical and Biological Engineering from Seoul National University in 2012. He completed postdoctoral studies in Korea Institute of Science and Technology (2015). He moved to Chungnam National University in 2015 and became associate professor of the Graduate School of Energy Science and Technology in 2019. His research interests include novel electrocatalysts for electrochemical energy conversion systems such as fuel cells and water electrolysis.

Published on 19 2564. Downloaded on 1/2/2569 7:34:44.

are systematically described. Furthermore, the scientific achievements in the application of M@C NPs to water electrolysis and fuel cell reactions are introduced, and the effects of the carbon encapsulation on the electrochemical reactions are rationally explained. The most recent advances in M@C catalyst structures for water electrolysis and fuel cell applications are expected to have a significant impact on future work towards the development of new types of electrocatalysts.

2. Fabrication of carbon shell-encapsulated metal (M@C) nanocatalysts

2.1 Chemical vapour deposition (CVD)

CVD is one of the most common and reliable methods for synthesizing TM-based single and bimetallic M@C core–shell structured materials.[57–66] A typical CVD method involves passing volatile carbon precursors on a metal-coated substrate. The carbon precursors are decomposed on the metal surface at high temperature, providing carbon sources to form a thin carbon shell at a controlled gas flow rate.[67] The physicochemical property and morphology of M@C materials fabricated *via* CVD methods depend on several factors such as the gas flow rate, temperature, chamber pressure, carrier–gas type, and precursor material.[68,69] For instance, in the fabrication of N-doped carbon shell-encapsulated NiMo NPs on 3D N-doped graphene using a two-step CVD process for the HER,[70] pyridine was used as the carbon and nitrogen sources to form an N-doped carbon shell on NiMo NPs (Fig. 1a). Through the 1st CVD process, annealing $NiMoO_4$ nanofiber under an Ar/H_2 atmosphere along with pyridine followed by etching $NiMoO_4$ yielded a porous 3D N-doped graphene substrate. In the 2nd CVD after Ni/Mo deposition on the substrate, well-dispersed NiMo@C NPs on the conductive graphene substrate were obtained.

2.2 Polymer coating coupled thermal treatment

Polymer coating methods have been extensively developed particularly for synthesizing M@C materials composed of Earth-abundant metals.[71–76] This method involves direct introduction of polymers (*e.g.*, polyvinylpyrrolidone (PVP), polydopamine (PDA), polypyrrole, *etc.*) to the metal precursor solution at ambient temperature or at slightly elevated temperature, and the polymer-blended precursor solution is then subjected to pyrolysis or calcination/annealing at a desired temperature to yield carbon shell-coated metal NPs.[68,69,71–77] The role of the polymers is to provide carbon sources for carbon shell formation on metal NPs. In addition, N-containing polymers can facilitate N doping on the outer carbon shell as well as carbon supports (CNTs, CNF, *etc.*), as depicted in Fig. 1b1.[72] Alternatively, Sung *et al.* fabricated intermetallic ordered face-centered tetragonal (fct)-PtFe NPs with tunable N-doped carbon shell layers by thermal treatment of PDA-coated carbon-supported PtFe (PtFe/C) (Fig. 1b2). By controlling PDA coating time, the carbon shell thickness can be modified, and an appropriate carbon coating layer (<1 nm thickness) prevents aggregation, coalescence, or dissolution of PtFe NPs during fuel cell operation while simultaneously retaining high activity.[51]

2.3 Solvothermal coupled thermal treatment

Solvothermal methods to prepare M@C NPs have been of intense interest due to numerous advantages including a low-temperature process (<300 °C), morphology tuning, scale-up, less-time consumption, carbon shell engineering, and so on.[47,48,78–83] Jung *et al.* have pioneered the synthesis of various TMs encapsulated by carbon shells including Earth-abundant TMs and noble metal/alloy-based catalysts such as Pt, Pd, Co, PtRu, PtFe, and PdAu,[47,48,78–83] which involves decomposing metal precursors (*e.g.*, metal acetylacetonates) in organic solvents with surfactants under inert atmospheres. The role of surfactants is to minimize particle agglomeration and control the size distribution and in some cases they are used as N-dopants.[47,48,83] The decomposition temperature is kept below 300 °C, after which the products are processed and subjected to annealing under different gas conditions to yield different M@C structures. For example, Fig. 1c depicts the preparation of carbon supported graphene-encapsulated Co NPs (Co@G/C) for the ORR through a solvothermal route.[47]

2.4 High-temperature pyrolytic methods

A high-temperature pyrolytic method is also one of the prevalent methods to fabricate M@C core–shell materials.[52,54,56,84–102] Pyrolysis methods involve the heat treatment of precursor compounds at high-temperatures (>500 °C) under inert gas atmospheres (*e.g.*, N_2 or Ar) wherein the precursor containing metal organic frameworks (MOFs) decompose to release simple volatile molecules (CO_2, nitrates, sulphur oxides, NH_3, volatile organic vapors, *etc.*), leaving a carbon material as a support (or frame) with carbon-encapsulated metals or alloys.[56,68,69,84–88] In particular, pyrolysis is widely used for the synthesis of

Sung Jong Yoo

Sung Jong Yoo obtained his Ph. D. degree from the School of Chemical and Biological Engineering at Seoul National University in 2009 and moved to KIST (Korea Institute of Science and Technology) for postdoctoral research. He began his independent career in 2012 as a senior research scientist in the Fuel Cell Research Center at KIST. He is currently a principal scientist at the Center for Hydrogen & Fuel Cell Research of KIST. His current research interests include: (i) the influence of surface chemistry of metal nanoparticles on catalytic activities and stability, (ii) the design principles for oxygen reduction activity of oxide catalysts for fuel cells, and (iii) the catalytic activity trends of the oxygen reduction reaction for alkaline anion exchange membrane fuel cells.

This journal is © The Royal Society of Chemistry 2021

Published on 19 2564. Downloaded on 1/2/2569 7:34:44.

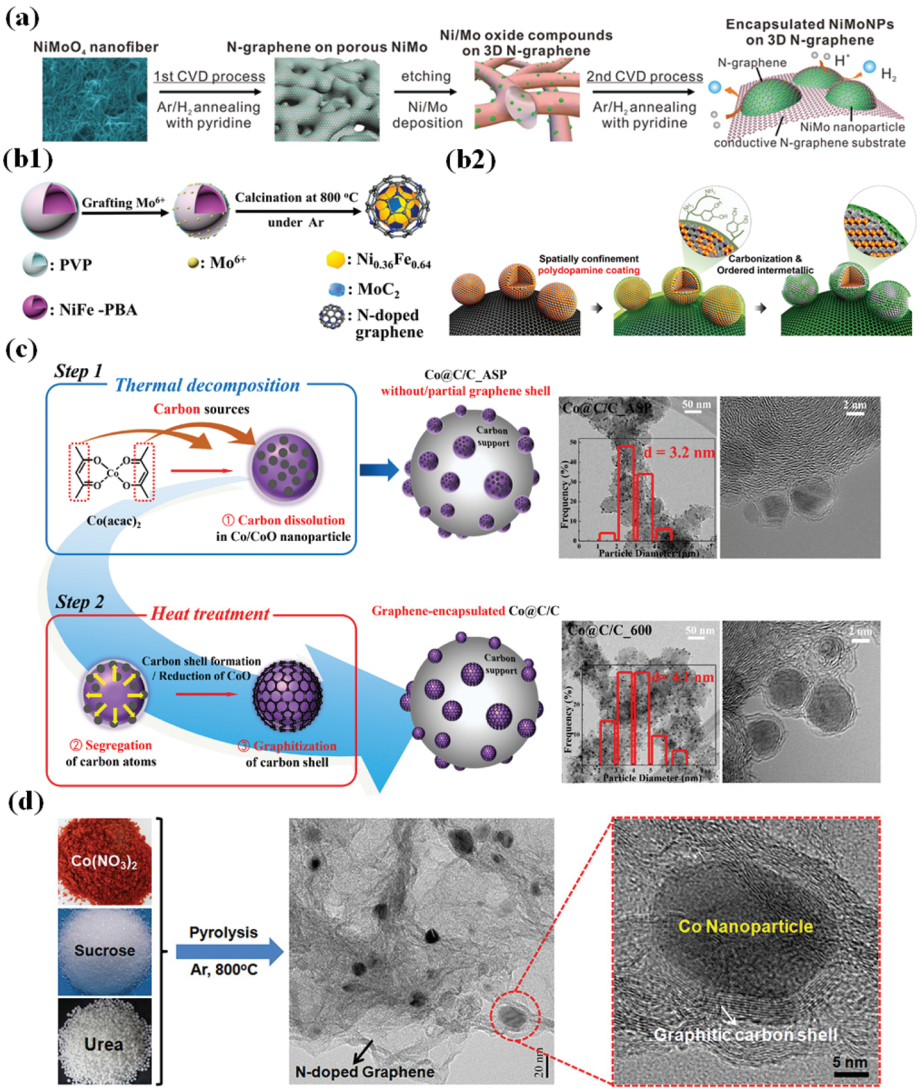

Fig. 1 Schematic illustration of the synthesis of the metal/metal alloy encapsulated carbon shell by various strategies. (a) Preparation of N-doped graphene-encapsulated NiMo NPs *via* a two-step CVD approach, adapted from ref. 70 with permission from ACS, copyright 2018. (b1) Synthesis of MoC_2-doped NiFe alloy NPs encapsulated within N-doped graphene *via* a polymer coating method, adapted from ref. 72 with permission from Elsevier, copyright 2018. (b2) Synthesis of carbon-supported and N-doped carbon-coated ordered intermetallic fct PtFe/C, reproduced with permission from ref. 51, ACS, copyright 2018. (c) TEM images of Co@G/C_ASP and Co@G/C_600 showing partial and complete encapsulation of Co NPs, reproduced with permission from ref. 47, RSC publications, copyright 2019. (d) Schematic illustration of the preparation of Co/N–C hybrids, adapted from ref. 92 with permission from Elsevier, copyright 2016.

metal NPs with heteroatom-doped carbon framework catalysts,[52,63,86,92,94,100] for example, calcination of carbon precursors containing metal species with hetero-dopant sources (melamine, H_2S, urea, sodium hydrogen phosphate, *etc.*) (Fig. 1d).[68,69,91,92] Inspired by the pioneering work of Jasinski's in 1964, wherein metal-phthalocyanines as metal macrocycles were converted to metal/N-doped carbon (M–N–C, M = Fe, Co, Ni) catalysts upon pyrolysis under inert conditions which were reported to show enhanced ORR performance,[89] thereafter, the synthetic protocols of fabricating M–N–C based electrocatalysts were widely adopted and extended to fabricate various inexpensive M–N–C electrocatalysts, reported as the best alternatives to Pt-based catalysts.[68,101,102]

3. Effects of the carbon shell and metal core on physicochemical properties of M@C catalysts

3.1 Electronic effects

The effect of core metals on the electronic structure of carbon shells is shown in Fig. 2. First of all, Kelly *et al.* reported the result of density functional theory (DFT) calculations for single graphene layer-coated metal surfaces.[103] A graphene formed on TM substrates exhibits an n- or p-type character depending on the nature of the metal. For instance, graphene that strongly interacted with a Co, Ni, Pd, or Ti substrate has an

Published on 19 2564. Downloaded on 1/2/2569 7:34:44.

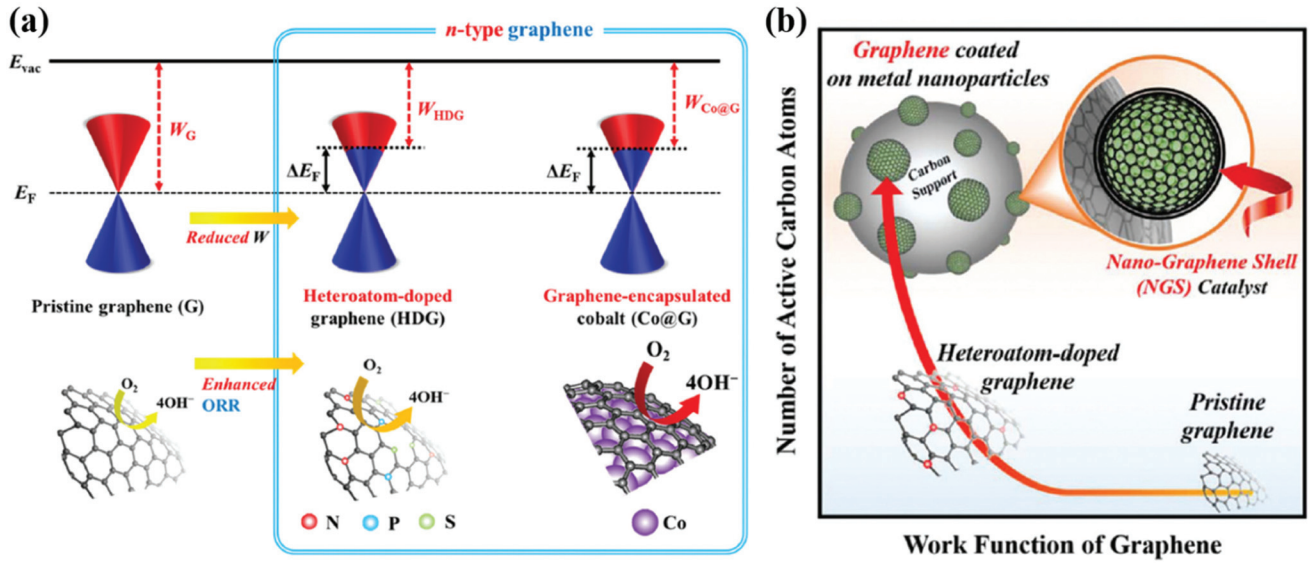

Fig. 2 Schematic illustration of the electronic effects between the carbon shell and metal nanoparticles (a) Design concept to modify the work function of the carbon shell *via* Co encapsulation, adapted from ref. 47 with permission from RSC publications, copyright 2019. (b) Advantages of carbon shell encapsulated Pd nanoparticle catalysts, adapted from ref. 48 with permission from RSC publications, copyright 2019.

n-type character while the work function of graphene on Pt or Au can change to a p-type due to weak interaction between them. Based on these results, for M@C NPs, the work function of the carbon shell is expected to be controlled depending on the type of core metal. Inspired by the previous studies, Jung *et al.* fabricated Pd@C and Co@C NPs with finely tuned carbon shells for the ORR in alkaline solutions.[47,48] It has been clearly observed that electrons are transferred from the core metal to the carbon shell, forming an n-type graphene catalyst. The charge transfer between the core metal and carbon shell can be facilitated due to the large electronegativity difference and the short distance (strong interaction) between them. As a result, the work function of the carbon shell is reduced through strong interaction with the electron-donating metal NP, resulting in an electronic structure suitable for the ORR. The catalytic activity of the carbon shell can be further improved through doping of heteroatoms, mainly nitrogen.[49,50,52,53] Chung *et al.* prepared N-doped carbon shell-coated PtFe NPs *via* polymer coating methods using N-containing polymers such as PDA followed by heat treatment for carbonization. The N-doped carbon shell provided additional active sites along with PtFe alloy NPs. By X-ray photoelectron spectroscopy (XPS), it was revealed that the structure of N-doped carbons (*e.g.*, pyridinic N, graphitic N, pyrrolic N, *etc.*) has an effect on the activity of the carbon shell.[51] However, it has been reported that the doping level is limited to less than 5 wt% since the doping process requires a high-temperature annealing enough to break the N–C bonds.

3.2 Structural effects

It is well known that the thickness and porosity of the carbon shell are very important factors affecting the performance of M@C NPs for electrochemical catalysis. In addition, the stability of M@C NPs is strongly affected by the crystallinity of the carbon shell. During electrochemical reactions, the thicker the carbon shell and the more crystalline, the more durable, but less active. Chung *et al.* demonstrated the effects of the thickness of carbon shells on the ORR activity of Pt-based NPs. Highly porous carbon shells can also provide a sufficient number of active metal surfaces, but metal NPs inevitably suffer from dissolution of 3d TMs, causing performance degradation. If the carbon shell is the main active site, not the core metal, the carbon shell thickness should be very thin, less than ~3 layers, since the charge transfer from the metal core to the carbon shell decreases exponentially as the thickness increases.[51]

However, the finely controlled pore structure of the carbon shell improves reaction selectivity since it can provide a molecular sieve effect. For instance, a carbon shell with extremely small pores selectively allows the permeation of H_2 gas rather than O_2 due to the difference in the kinetic diameter. Using the molecular sieve effect by the carbon shell, Jung *et al.* developed HOR-selective Pt@C/C catalysts with high durability under shut-down-start-up conditions during fuel cell operation.[80] Accordingly, fine control of the carbon shell structure is the most important technique for developing electrocatalysts suitable for each purpose (Fig. 3).

4. Applications of metal@carbon core–shell catalysts to water electrolysis and fuel cell reactions

4.1 Direct utilization of carbon shells as active sites

4.1.1 Hydrogen evolution reaction (HER). In the HER process, some of the non-noble TMs show high performance comparable to that of noble metals. However, under harsh conditions such as strong acid or alkaline solutions, they do not demonstrate sustainable activity due to their low conductivity and poor stability.[104]

 This journal is © The Royal Society of Chemistry 2021

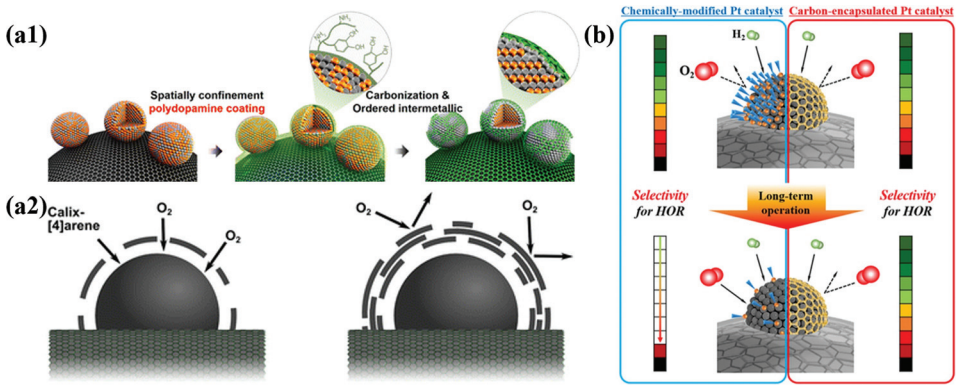

Fig. 3 Schematic illustration of structural effects for carbon shell on metal nanoparticles (a1) Synthesis of N-doped carbon shell-coated ordered PtFe nanoparticles (a2) Effect of O_2 permeability *via* carbon shell thickness for electrochemical activity, adapted from ref. 51 with permission from ACS, copyright 2015. (b) Schematic illustration of HOR selectivity change of Pt catalyst and carbon encapsulated Pt catalyst during PEMFC operation, with permission from ref. 80, ACS copyright 2019.

Published on 19 2564. Downloaded on 1/2/2569 7:34:44.

Therefore, complete metal encapsulation by a carbon shell protects the TM NPs from harsh conditions because the embedded metal NP is not directly exposed to the electrolyte solutions. Furthermore, as supported by many experimental and theoretical calculation results,[57,68,69,105–108] the electrochemical HER can be simultaneously triggered on the carbon surface due to the modification of the electronic structure by electron transfer from the core metal to the carbon shell. However, as mentioned earlier, the catalytic activity of M@C NPs strongly depends on the composition of the core metal and the thickness and crystallinity of the carbon shell.[57,107] The HER performances of various carbon shell-encapsulated metal/alloys are summarized in Table 1.

Laasonen *et al.* demonstrated this phenomenon in a chain-mail type catalyst composed of Fe NPs completely encapsulated in graphene single shell layers (SCEIN) supported on single walled carbon nanotubes (SWCNTs) (Fig. 4a1), exhibiting high HER electrochemical activity on the graphene surface influenced by encapsulated Fe NPs with good stability in an acidic solution. It was revealed that the catalyst showed an onset potential of 0 V *vs.* RHE, which is close to the thermodynamic potential of the HER, and a low overpotential of 77 mV to reach $j = 10$ mA cm^{-2} almost similar to that of Pt/C (Fig. 4a2).[66]

Experimental and theoretical investigations prove electron transfer from Fe to the graphene surface due to the difference in the work function, which increases the density of states

Table 1 Summary of HER electrochemical parameters of various metal and metal alloy encapsulated graphene layers

Catalysts	Synthetic method	Electrolyte	Overpotential (mV)@10 mA cm^{-2}	Tafel slope (mV dec^{-1})	Stability (cycle or hours)	Ref.
Co@NC	Hydrothermal-CVD	0.5 M H_2SO_4	265	98	1000	57
NiCu@C	Sol–gel/CVD	0.5 M H_2SO_4	48	63	2000	61
Fe@single shell	CVD	0.5 M H_2SO_4	77	40	1000	66
NiMo-G	CVD	0.5 M H_2SO_4	56	49	24 h	70
Co@BCN	Hydrothermal-annealing	0.5 M H_2SO_4	96	63.7	2000	71
MoC_2-doped carbon	Calcination	1.0 M KOH	320	31	10 000	72
3D Cu@N/CNTs	Pyrolysis	1.0 M KOH	123	63	10 h	73
FeCo@N-graphene	CVD	0.5 M H_2SO_4	262	74	10 000	76
Co@N-doped carbon	Pyrolysis	1.0 M $HClO_4$	200	100	10 000	86
NiRu@N–C	Pyrolysis	0.5 M H_2SO_4	50	36	1000	90
FeCo@N-graphene	Pyrolysis	1.0 M KOH	233	102	1000	91
IrNi@OC	Pyrolysis	1.0 M KOH	27	50	12 h	96
CoNi@NC	Hydrothermal-annealing	0.5 M H_2SO_4	142	104	1000	113
Ni_2P@PCG	Solvothermal-annealing	0.5 M H_2SO_4	110	59	5000	115
PdCo@N-graphene	Pyrolysis	0.5 M H_2SO_4	80	31	10 000	117
FeCo@Graphene	Pyrolysis	1.0 M KOH	149	77	10 000	119
Co@N-CNTs	Pyrolysis	0.5 M H_2SO_4	260	69	8.5 h	146
Co@C	Hydrothermal-annealing	1.0 M KOH	90	91	5000	177
CoFe@N-graphene	Pyrolysis	1.0 M KOH	272	96	1000	178
FeCo@N–C	Pyrolysis	0.5 M H_2SO_4	230	92	5000	179
CoP/CO_2P@NC	Pyrolysis	0.5 M H_2SO_4	126	79	1000	192
Ni@porous carbon	Carbonization	0.5 M H_2SO_4	105	72	500	193
FeCoNi@NC	Lyophilization-pyrolysis	1.0 M KOH	175	168	1000	194
NiCo@N–C	Pyrolysis	1.0 M KOH	68	180	2000	195
IrCo	Hydrothermal-annealing	0.5 M H_2SO_4	24	23	10 000	196

Published on 19 2564. Downloaded on 1/2/2569 7:34:44.

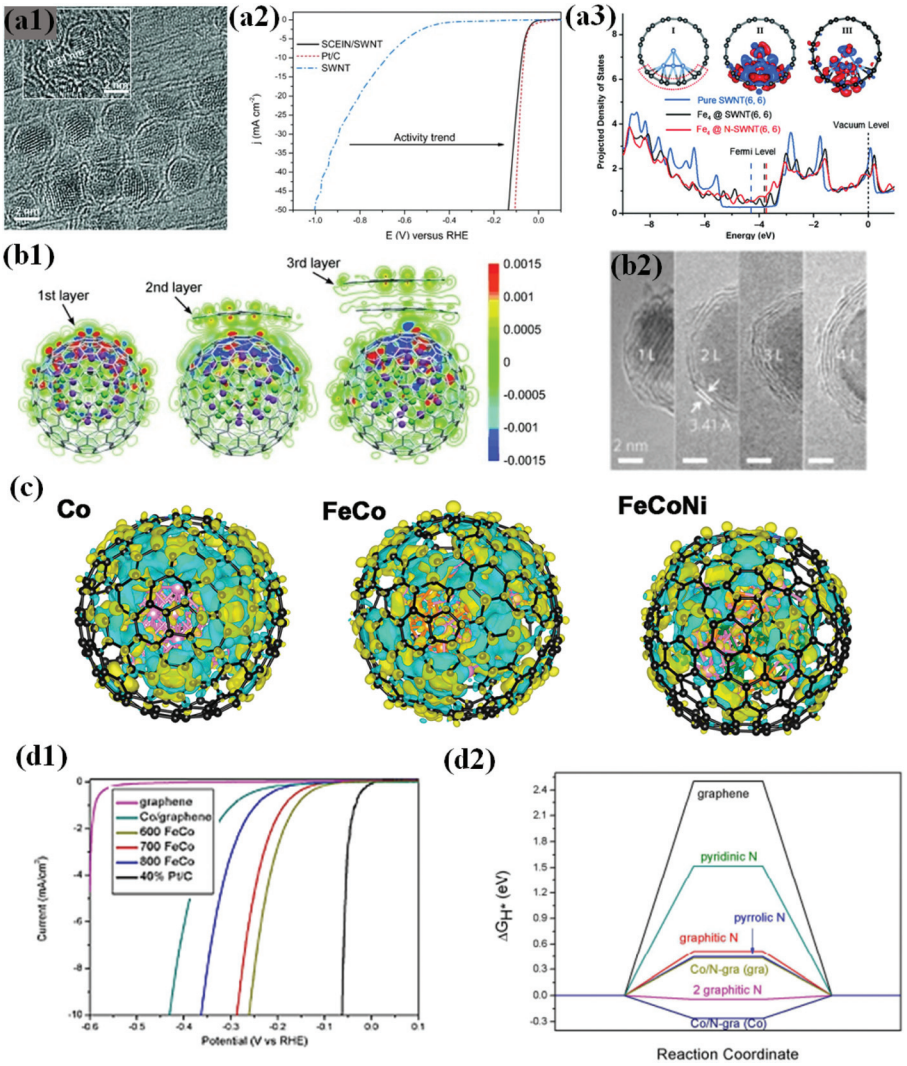

Fig. 4 (a1) HRTEM image of the SCEIN/SWNT sample, the inset indicates the (110) lattice plane of the Fe particles in Science. (a2) Polarization curves of SWNT (blue), SCEIN/SWNT (black), and Pt/C (red). The polarization curves were measured at a scan rate of 50 mV s^{-1} in 0.5 M H_2SO_4, reproduced with permission from ref. 66, Wiley publications, copyright 2015. (a3) Projected DOS of the p orbitals of C atoms bonded to Fe_4 in Fe_4@SWNT and Fe_4@N-SWNT compared with that in pure SWNT. Inserted plot I and plot II show the optimized structure of Fe_4@SWNT and its difference charge density, and plot III corresponds to that of Fe_4@N-SWNT. The red and blue regions in plots II and III indicate a charge increase and decrease, respectively, reproduced with permission from ref. 109, Wiley publications, copyright 2018. (b1) HRTEM images of CoNi@NC, showing the graphene shells and encapsulated metal NPs. Inset: Crystal (111) plane of the CoNi alloy. (b2) Redistribution of the electron densities after the CoNi clusters are covered by one to three layers of graphene. The red and blue regions are regions of increased and decreased electron density, respectively, reproduced with permission from ref. 113, Wiley publications, copyright 2015. (b3) High-resolution transmission electron microscopy (HRTEM) images of FeCo NPs covered by one to four layers of graphene (1–4 L), reproduced with permission from ref. 114, RSC publications, copyright 2013. (c) Calculated charge density differences of various models. The isosurface value of the color region is 0.01 e $Å^{-3}$. The yellow and cyan regions refer to increased and decreased charge distributions, respectively. FeCoNi ($Fe_{24}Co_{24}Ni_7$) refers to ternary alloys with lower and higher Ni contents, respectively, reproduced with permission from ref. 119, ACS publications, copyright 2017. (d1) Polarization curves of different FeCo annealed samples measured at a scan rate of 50 mV s^{-1} in 0.5 M H_2SO_4 solution. (d2) Calculated ΔG_{H^*} diagram of some models; the words in the bracket mean the H* adsorbed on whether graphene or Co_4 side, reproduced with permission from ref. 76, RSC publications, copyright 2015.

(DOS) near the Fermi level of graphene and decreases the local work function of graphene (Fig. 4a3). Consequently, n-type graphene promotes the electrocatalytic reaction on the graphene surface.[109–112] The electronic modulation of the graphene shell by inner metals/metal alloys has been realized in many catalytic systems ranging from Earth-abundant TMs to noble metal-like groups.[69,90,113] Of note, there are several factors that can affect the electronic communication between metal and graphene, including graphene layer thickness, doped heteroatom, metal or alloy composition, and nanostructure of metal encapsulation.[65]

In particular, numerous studies have shown that the carbon shell thickness is tunable by optimising the preparation conditions, which in turn affects the number of electrons transferred and subsequent electronic alteration.[61,104,105,107] To improve the HER activity of carbon-encapsulated NPs, the carbon shell thickness should not be more than 3 to 4 layers,

 This journal is © The Royal Society of Chemistry 2021

Published on 19 2564. Downloaded on 1/2/2569 7:34:44.

i.e., electron penetration efficiency increases with decreasing layer thickness (Fig. 4b1 and b2).[114] The best HER activity could be achieved by confining the NP in single shell encapsulation for efficient electron transfer.[66,113] However, the single carbon shell might not provide high robustness and slowly tend to decline in activity, resulting in low stability during a long-term operation, while some studies indicate the formation of a partially oxidized state of the metal surface.

A number of DFT studies suggest that charge transfer takes place between the inner core and outer carbon shell, and the charge transfer can be further modified by alloying with heteroatoms caused by ligand or strain effects,[71,115–118] which in turn affects the charge densities in the carbon network by the difference in the number of electrons transferred. Since electrocatalytic reactions occur at the carbon shell surface, the change in the electronic structure of the carbon shells can be evaluated by Bader charge analysis and several studies support the evidence that single metal, binary, and ternary alloy core materials exhibit different charge densities.[59,61,68,76] Accordingly, the electronic structure of the outmost carbon shells also varies, affecting the binding energy of the reaction intermediates. For instance, Fig. 6c shows different charge densities of Co, FeCo, and FeCoNi encapsulated by the carbon shell. Among them, carbon shell-coated FeCoNi exhibits superior HER activity (η_{10}: 149 mV *vs.* RHE) to their binary and single counterparts.[119]

One can also tailor the catalytic activity by changing the structure of the carbon shell. For example, doping of heteroatoms such as N, P, F, S, and B has proven to be effective in further tuning the electronic property and catalytic performance.[71,75,76,115] Importantly, among the dopants, N doping in a carbon matrix is prevalent among core–shell structured materials due to numerous advantages.[68,107,108]

Doping N into a graphene matrix increases the DOS near the Fermi level and improves HER performance by decreasing ΔG_{H^*} close to zero which is the key indicator to probe HER activity.[76] Intriguingly, increasing the N dopant level further maximizes HER performance by optimizing the electronic properties of graphene.[76,104,105,107] Chen *et al.* found that an appropriate annealing temperature for the FeCo-MOF precursor resulted in a high doping level of N (8.2 at%) in carbon shell-coated bimetallic FeCo alloy NPs, exhibiting much enhanced HER activity with a low η_{10} of 262 mV *vs.* RHE (Fig. 4d1). Their DFT calculations indicated that an appropriate increase in N doping increases the H adsorption sites and decreases ΔG_{H^*}, thereby showing superior HER performance (Fig. 4d2).[76] In addition, a few studies have observed a significant increase in HER activity by co-doping N and B in the carbon shell, leading to a more optimized electronic structure of the carbon surface and synergistically coupling with the encapsulated metal NPs to promote high HER activity.[68,71,106]

Utilizing carbon shells as active sites is not restricted to non-noble metals, but has been also studied in various carbon-coated noble metals and their alloy systems. Ultralow loading of noble metals with other non-noble metals can maintain intrinsic high activity and reduce material cost.[98,116–118,120] In this regard, coupling noble metals like Ru with 3d TMs to form bimetallic alloys has been a promising way to fabricate highly active bimetallic catalysts, and it was revealed that the surface properties, charge distribution, strain and ligand effects can be also modified similarly to non-noble metal-based M@C catalysts.[98,116–118]

Su *et al.* reported high HER activity of RuCo alloy catalysts exceeding the activity of Pt/C, showing that they are economically advantageous over other Pt group metals. Their DFT calculations suggest that alloying Co with a small amount of Ru can enhance the HER activity comparable to a pure Ru catalyst through more electron transfer from the RuCo alloy core to the outer carbon shells and enhanced C–H bonds, thereby lowering ΔG_{H^*} for efficient catalytic activity.[197] Similarly, Xu and co-workers fabricated NiRu alloys encapsulated by N-doped carbon, exhibiting superior HER activity close to Pt/C in acid solutions.[100] Besides, Pd has a strong affinity for H adsorption; thus, Pd-based materials are widely used as primary catalysts for electrocatalytic HER applications. Therefore, Chen *et al.* designed N-doped graphene-encapsulated PdCo systems and reported that high conductivity of the graphene layer and N-doping enhanced the charge transfer and the number of active sites.[117,121,122]

4.1.2 Oxygen evolution reaction (OER). One of the half-reactions of water electrolysis, OER, is kinetically sluggish and requires noble metal-based catalysts such as RuO_2 or IrO_2 to lower overpotential and to enhance activity; however, poor stability of noble metal catalysts due to metal dissolution under harsh redox conditions makes commercialization unfavorable.[123,124] Therefore, the development of Earth-abundant noble metal-free catalysts is highly important, but their low OER efficiency calls for the development of new strategies to improve the catalytic activity.[125,126] In this regard, the concept of carbon shell encapsulation of metal or metal alloy NPs has been adopted to develop highly efficient and durable OER catalysts. However, it is very important to identify the main active sites, since only the surface of the carbon shell is exposed to the electrolyte.[106,107,109,127] The identification of the carbon shell as active sites has been supported by numerous theoretical studies claiming that the outer inert carbon layer can be activated primarily due to electronic interaction with metal NPs. However, there is insufficient experimental evidence to prove the carbon shell as an active site. The recently reported OER performances of carbon shell-encapsulated metal/alloys are summarized in Table 2.

Bao and co-workers attempted to find reliable evidence for the electronic interaction between carbon shells and encapsulated metal NPs through direct chemical imaging and spectral analysis using scanning transmission X-ray microscopy (STXM). Furthermore, they used X-ray absorption near edge structure (XANES) and computational simulation study to support the STXM results.[128–130] In their study, the STXM chemical image (Fig. 5a1) shows Fe NP encapsulated pod-like carbon nanotubes (Pod-Fe) consisting of three different regions: Fe particle regions, thick CNT regions, and thin CNT regions, marked by red, green, and blue, respectively. In STXM XANES spectra for the three different regions, changes in the C 1s graphitic domains of π^* (285.2 eV) and σ^* (~292 eV) were

Published on 19 2564. Downloaded on 1/2/2569 7:34:44.

Table 2 Summary of OER electrochemical parameters of various metal and metal alloy encapsulated graphene layers

Catalysts	Synthetic method	Electrolyte	Overpotential (mV)@10 mA cm^{-2}	Tafel slope (mV dec^{-1})	Stability (cycle or hours)	Ref.
Porous CoNi@NC	Solvothermal	0.1 M KOH	500	66	1000	54
FeCo@NC/NCNTs	Calcination	0.1 M KOH	355	57	60 h	58
FeNi@NC	CVD	1.0 M NaOH	280	70	10 000	65
MoC_2-doped NiFe@C	Calcination	1.0 M KOH	320	31	10 000	72
FeCo@N-graphene	Pyrolysis	1.0 M KOH	380	99	1000	91
Ni@N-doped C	Precipitation	1.0 M KOH	280	45	1000	94
FeCoNi@graphene	Pyrolysis	1.0 M KOH	288	60	10 000	119
NiFe–N/C	Template-free pyrolysis	0.1 M KOH	320	44	2000	131
NiFe@C	Electrical explosion	1.0 M KOH	274	57	5000	133
NiCo@BC	Ultrasonic stripping	1.0 M KOH	309	62	1000	147
NiFe@NCNFs	Electrospinning	1.0 M KOH	294	52	2000	148
Co/FeC@NC	Polymer coating	1.0 M KOH	380	70	1000	151
FeCo–N/PC	Solution-impregnation	0.1 M KOH	395	68	3000	171
NiFe-G	Sol–gel/carbothermal	1.0 M KOH	280	43	10 h	176
Co@NC	Pyrolysis	1.0 M KOH	400	108	10 000	186
FeNi@C/NG	Calcination	0.1 M KOH	430	105	2000	190
FeCo@NC	Ball milling	0.1 M KOH	440	90	1000	191
FeCoNi@NC	Lyophilization-pyrolysis	1.0 M KOH	270	60	1000	194
FeCo@NC	Electrospinning	1.0 M KOH	283	38	53 h	198
3D NiCo@NCNTs	Pyrolysis	0.1 M KOH	41	177	1000	199
FeCo@NG/NCNT	Ball milling	1.0 M KOH	450	77	5.5 h	200
FeCoNi@NC	Pyrolysis	0.5 M KOH	400	72	10 h	201

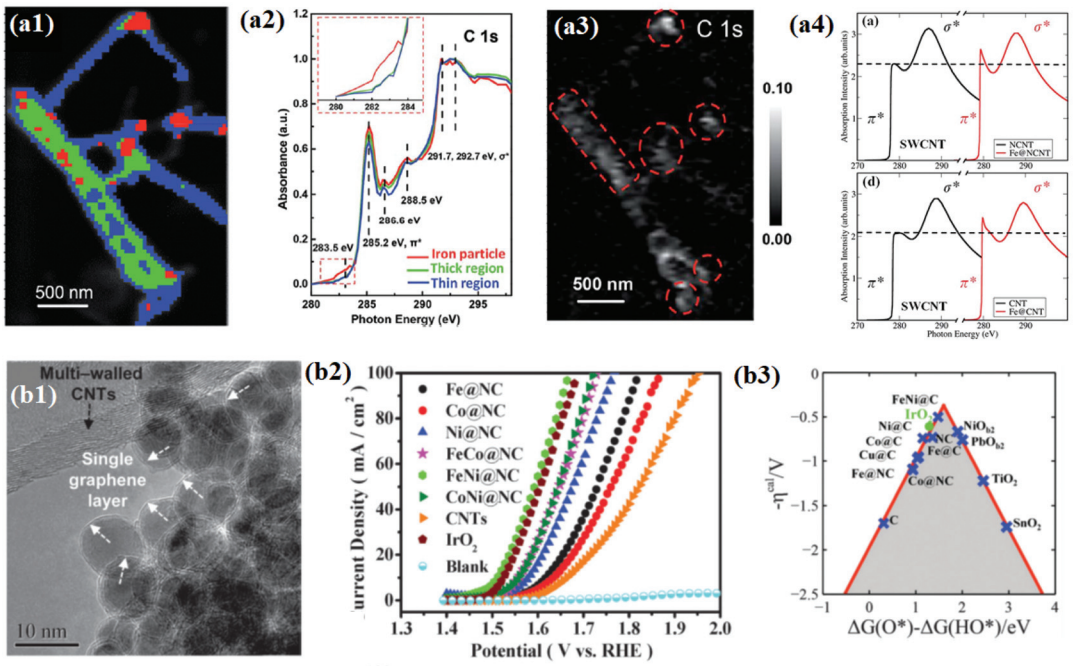

Fig. 5 (a1) STXM chemical images of the pod-like carbon nanotube with encapsulated iron (Pod-Fe). Color composite regions, red: iron particle regions; green: thick CNT regions; blue: thin CNT regions. (a2) STXM XANES spectra and mappings of C 1s on Pod-Fe. Selected regions on the sample to extract normalized C 1s XANES spectra from the STXM stack (normalization range from the lowest absorbance to the highest), the inset shows the magnified image of the dashed red rectangle. (a3) Pre-edge peak map at 283.5 eV, using the pre-edge peak averaged images (from 282.5 to 283.5 eV) subtracting the pre-edge averaged images (from 280 to 281 eV). The red dashed circles indicate the main iron particles' position. The scale bars on the right represent the absorbance intensity. (a4) Calculated X-ray absorption spectra of carbon atoms at the K-edge on CNTs with and without the Fe_4 cluster with the N dopant and undoped SWCNT, reproduced with permission from ref. 128, RSC publications copyright 2015. (b1) Morphology of metal@NCs and the white arrows in the inset show the single layer graphene, and the black arrow in the inset shows the multi-walled carbon nanotubes. (b2) Electrocatalytic OER performance test of M@NCs in O_2-saturated 1 M NaOH solution at 25 °C OER polarization curves for metal@NCs in comparison with CNTs and IrO_2 with the same mass loading. (b3) Calculated negative overpotential (η^{cal}) against the universal descriptor $\Delta G(O^*) - \Delta G(HO^*)$ on different catalysts, reproduced with permission from ref. 65, RSC publications copyright 2016.

This journal is © The Royal Society of Chemistry 2021

Published on 19 2564. Downloaded on 1/2/2569 7:34:44.

observed (Fig. 5a2). The increase in the intensity of the C 1s π^* signal (285.2 eV) in the Fe particle region (red) implies that Fe NPs might tune the electronic structure of the carbon shells. As shown in the simulated XAS spectra (Fig. 5a4), it was revealed that the increase in the intensity of π^* bonds of single-walled CNTs (SWCNTs) with encapsulated Fe was due to a decrease in the number of electrons in the anti-bonding orbital by electron transfer from Fe NPs to carbon shells. Furthermore, the electron transfer enhances the pre-edge signals at ~283.5 eV of the C 1s peak (Fig. 5a2), and the corresponding mapping image (Fig. 5a3) shows white dots at the same location as the Fe NPs marked in red in Fig. 5a1. The analysis results clearly demonstrated the electronic interaction between Fe and the carbon shell which improves the adsorption of oxygen containing species (O, OH, OO, and OOH) as reaction intermediates for the OER.

The understanding of the electronic interaction and the identification of the main active sites have led to the development of various 3d TMs and their alloys with core–shell structured materials for OER applications.[65,105,107] The same group pioneered the synthesis of N-doped single layer graphene-encapsulated 3d TM NPs (M@NC) such as Fe, Co, Ni, and their alloys using a CVD process (Fig. 5b1). Electrochemical measurements of different types of M@NC catalysts revealed the OER activity trend in the order of FeNi@NC > CoNi@NC > FeCo@NC > Ni@NC > Co@NC > Fe@NC. In addition, for 10 000 cycles, the optimized FeNi@NC catalyst exhibited superior stability compared to a commercial IrO_2 catalyst in alkaline solutions (Fig. 5b2).[65] Finally, the DFT calculation showed that by tuning the metal compositions, the OER activity descriptor, $\Delta G(O^*) - \Delta G(HO^*)$, could be optimized and consequently the highest activity of the graphene layer could be found (Fig. 5b3). These observations conclude that the electronic transformation of the inert graphene shell also facilitates oxygen electrocatalysis, as observed for the HER.

Other research groups demonstrated a similar catalytic phenomenon,[63,94,131–133] and some recent studies reported that apart from the graphene shell as active sites *via* modification of electronic structures, the *in situ* formed oxidized metal species synergistically contribute to OER activity.[63,94,131,133]

4.1.3 Oxygen reduction reaction (ORR). High-efficiency ORR catalysts for fuel cells have been extensively studied to overcome the sluggish reaction kinetics. Over the past decades, Pt has been used mainly as an ORR catalyst, but its commercialization is limited due to cost issues and lack of reserves. Accordingly, to reduce the amount of Pt used, Pt-based alloys and core shell catalysts have been investigated.[134–138] In addition, non-precious metal catalysts with a Pt-free M–N–C structure have been developed, showing high ORR activity comparable to Pt/C in half-cell tests. However, as mentioned earlier, M–N–C catalysts still have the disadvantages of lack of the number of active sites, low durability, and easy stacking.[139–145] In particular, it is difficult to make a porous electrode structure since the M–N–C catalyst is densely stacked when fabricating an electrode, which results in poor fuel cell performance.

In recent years, M@C catalysts with an appropriate carbon shell structure have been proposed to improve the activity and durability of non-precious metal-based materials and to make a novel catalyst structure applicable to unit cells. Researchers have initially studied TM NPs encapsulated by an N-doped carbon shell and tried to highlight the improved ORR activities of the novel catalyst structure. Wang *et al.* fabricated carbon-encapsulated Co NPs (Co@G) deposited on N-doped graphitic carbon nanosheets (N-GCN), which exhibited a half-wave potential of 0.94 V comparable to that of Pt/C due to the optimized balance of graphitic N and pyridinic N sites in both the nanosheet and carbon shell.[50] Similarly, Ning *et al.* synthesized CoNi@N–C *via* incorporating CoNi into ZIF followed by a high-temperature carbonization process.[51] The enhanced ORR activity of CoNi@N–C was elucidated by the synergistic interaction between the N-doped carbon shell and the CoNi surface making active sites, $CoNiN_x$.[54] However, at that time, very few studies understood the carbon shell as the main active site since most researchers believed that carbon materials do not have catalytic activity for electrochemical reactions.

For the first time, to clearly identify the main active site of M@C catalysts, Gewirth *et al.* investigated the change in the electrochemical properties of a catalyst containing both Fe@C NPs and Fe–N–C sites depending on the annealing gas atmosphere (Cl_2 and H_2).[87] Through the Cl_2 treatment, the metallic Fe (Fe@C) and FeN_4 (Fe–N–C) species are converted into $FeCl_3{\cdot}xH_2O$ that is reformed into reduced Fe species (Fe@C) by the H_2 treatment. Interestingly, the ORR activity decreased significantly after the Cl_2 treatment, but it recovered back to its initial state after the H_2 treatment. Therefore, it was concluded that the FeN_4 species do not affect the ORR activity, while the Fe@C NPs serve as the main active materials for the ORR. Furthermore, Jiang *et al.* synthesized N-doped carbon-encapsulated Fe_3C–Co NPs, and conducted DFT calculations to unravel the mechanism for improved ORR activity of M@C catalysts.[55] Combining with Fe_3C–Co, the π-bonds between N–C and C–C of N-doped carbon shell are weakened, which makes the OOH* bond to the carbon shell stronger and leads to easier OOH formation.

In recent years, the importance of controlling the work function of the carbon shell through charge transfer between the core metal and the carbon shell has emerged. As shown in Fig. 6a, Jung *et al.* developed carbon-supported Pd@C (Pd@C/C) catalysts without doping of heteroatoms and revealed that the ORR can be promoted when the work function of the carbon shell is reduced by charge transfer from the core metal NP to the carbon shell.[48] In addition, Yoo *et al.* reported a highly active and durable carbon-supported Co@C (Co@C/C) catalyst for the ORR (Fig. 6b), showing excellent AEMFC performance comparable to that of unit cells using Pt/C catalysts.[47] The improved ORR activity of the Co@C/C catalyst was attributed mainly to the reduced work function of the carbon shell (n-type graphene shells) and the 3D catalyst structure with Co@C NPs highly dispersed on a carbon support, maximizing the electrochemically active surface area even in a unit cell. In the previous studies, complete encapsulation of Pd NPs by carbon shells accelerates the charge transfer, which has been clearly demonstrated in in-depth XPS studies. Fig. 7a also shows that the main active site of the Pd@C/C catalyst is only the carbon shell, not the Pd surface, *via* the Pd poisoning

Published on 19 2564. Downloaded on 1/2/2569 7:34:44.

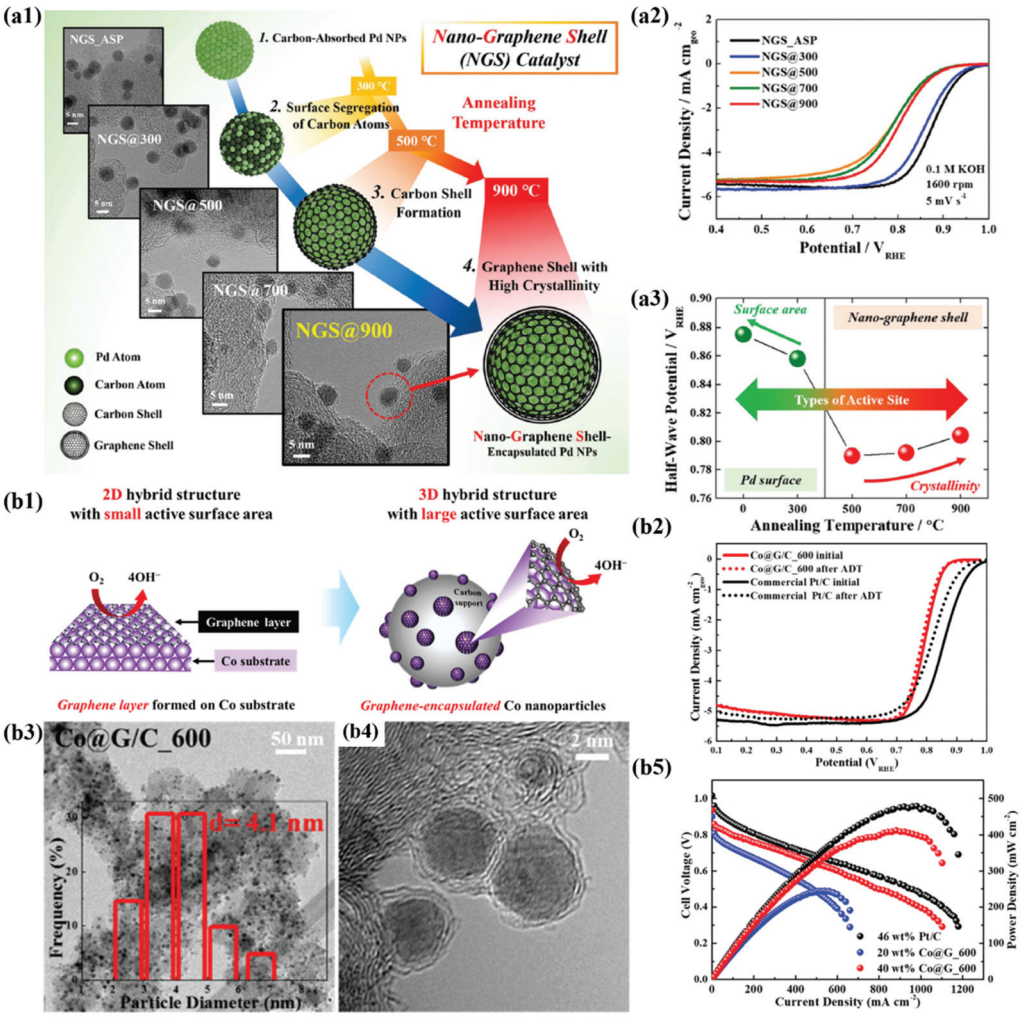

Fig. 6 (a1) Structural changes of NGS catalysts based on TEM images at different annealing temperatures (300–900 °C). (a2) ORR polarization curves of NGS catalysts. (a3) Correlation between half-wave potential and heat treatment temperature, reproduced with permission from ref. 48, RSC publications copyright 2019. (b1) Schematic diagram of the maximized active site of Co@G/C *via* the 3D structure of the carbon shell (b2) ORR polarization curves of Co@G/C. (b3, 4) TEM images of Co@G/C_600. (b5) MEA performances of Co@G/C_600 in AEMFC, reproduced with permission from ref. 47, RSC publications copyright 2019.

test using organic molecules with thiol groups. For the Co@C/C catalyst, the CN^- adsorption/desorption (poisoning/washing) tests clearly prove that the active sites of the Co@C/C catalyst are the carbon shells, not the Co surface (Fig. 7b). Furthermore, it is demonstrated that the carbon shell can play a role of a protective layer to prevent dissolution of the core Co NPs during fuel cell operation (Fig. 6b2).

Accordingly, M@C catalysts with highly active and durable carbon shells are considered promising ORR catalysts to overcome the disadvantages of M–N–C catalysts. Table 3 shows the recently reported electrochemical properties (ORR activity and durability) of M@C catalysts, mainly focusing on AEMFC applications.

4.2 Highly durable catalysts encapsulated by carbon shells as protective layers

4.2.1 Hydrogen evolution reaction (HER). In general, noble metal-based HER catalysts show poor stability during long-term operation due to dissolution under redox conditions.[69,123,124] Therefore, it is very important to develop a low-cost and Earth-abundant, and highly stable electrocatalyst for the HER as an alternative to increase economic feasibility. For example, 3d TMs such as Fe, Co, or Ni and their alloys have shown excellent HER activity and durability in alkaline medium, but show poor durability in acidic medium, excluding their use in proton exchange membrane-based electrolysers.[68,98,108]

Some previous studies demonstrate that chainmail catalysts composed of non-precious earth-abundant metals/alloys supported on CNTs trigger electrochemical reactions on the outer carbon shell surface during water electrolysis, while carbon layers protect the metals against acid leaching/dissolution, thus enhancing durability in an acidic medium.[109,113,114] In the same context, Deng *et al.* developed highly active and durable Fe, Co, and FeCo alloy NPs encapsulated in CNTs

 This journal is © The Royal Society of Chemistry 2021

Published on 19 2564. Downloaded on 1/2/2569 7:34:44.

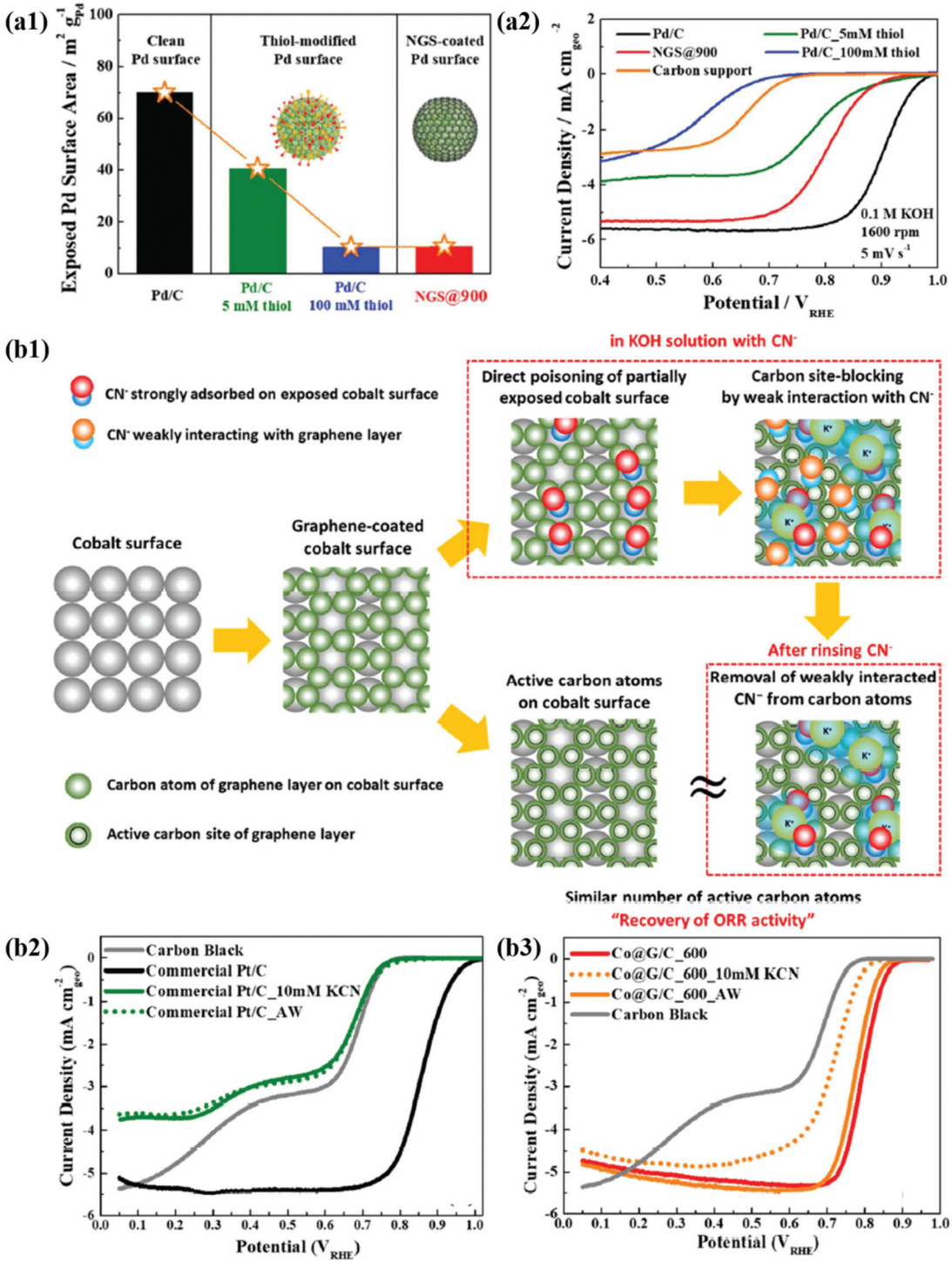

Fig. 7 (a1) The exposed Pd surface area of Pd@C. (a2) ORR polarization curves of Pd/C, Pd/C-5 mM thiol, NGS@900, Pd/C_100 mM thiol, and carbon support, reproduced with permission from ref. 48, RSC publications copyright 2019. (b1) Schematic illustration of the mechanism for CN^- effect on Co@G/C. (b2) ORR polarization curves of commercial Pt/C. (b3) Co@G/C in 0.1 M KOH with 10 mM KCN and after cleaning in pure 0.1 M KOH, reproduced with permission from ref. 47, RSC publications copyright 2019.

through a CVD method (Fig. 8a1).[59] In their work, the optimized FeCo NPs encapsulated in N-doped CNTs (FeCo@NCNTs) show high HER activity even in H_2SO_4 solution (Fig. 8a2). The FeCo NPs completely coated by rigid graphitic carbon shells are protected against surface oxidation and particle migration during a long-term durability test of 10 000 cycles, without any noticeable decline in HER activity (Fig. 8a3). Yang *et al.* observed similar results for FeCo@NC

Table 3 Summary of ORR electrochemical parameters of various metal and metal alloy encapsulated graphene layers

Catalysts	Synthetic method	Electrolyte	Overpotential (mV)@10 mA cm^{-2}	Tafel slope (mV dec^{-1})	Stability (cycle or hours)	Ref.
Co@G/C_600	Solvothermal	0.1 M KOH	0.80	—	5000	47
NGS@900	Solvothermal	0.1 M KOH	0.87	—	5000	48
O–Pd–Fe@NC/C	Pyrolysis	0.1 M KOH/0.1 M $HClO_4$	0.91/0.88	—	30 000/10 000	49
Co@G/N-GCNs	Pyrolysis	0.1 M KOH	0.84	70	2000/10 h	50
Fct–PtFe/C	Solvothermal	0.1 M $HClO_4$	0.93	—	10 000	51
PdCo@NPNCs	Pyrolysis	0.1 M KOH	0.90	49	5.6 h	52
Pd-PANI-K@500	Pyrolysis	0.1 M $HClO_4$	0.79	—	300	53
Co_2Ni_1@N–C	Calcination	KOH	0.82	63	4.2 h	54
Fe_3C–Co/NC	Pyrolysis	1 M KOH	0.885	—	16.7 h	55
NFC@Fe/Fe_3C-8	Ball milling	0.1 M KOH/0.1 M $HClO_4$	0.87/0.73	80/44	50 000/30 000	75
Fe/C_H_2-treated	Solvothermal	0.1 M $HClO_4$	0.63	—	—	87
Fe@N–C-700	Pyrolysis	0.1 M KOH	0.83	—	30 000	127
UsPtCu@C	Pyrolysis	0.1 M KOH	0.87	—	5000	160
Co_3O_4@C–N	Solvothermal	0.1 M $HClO_4$	0.37 (Ag/AgCl)	—	1000	163
CoNi/NG	Pyrolysis	0.1 M KOH	0.85	51	12 h	202
Ni@NCNTs-800	Pyrolysis	0.1 M KOH	0.83	84	2000	203
Fe_{30}@N/HCSs	Pyrolysis	0.1 M KOH	0.85	62	8.3 h	204
3C-900	Pyrolysis	0.1 M KOH	0.82	—	4.4 h	205

Published on 19 2564. Downloaded on 1/2/2569 7:34:44.

prepared by direct carbonization of the MOF precursor, $Fe_3[Co(CN)_6]_2$.[76] These studies provide insights into the electrochemical stability of Earth-abundant M@C type catalysts under acidic conditions during long-term operation.

Using different types of active materials, Chung and co-workers have revealed the importance of the carbon shell to enhance the durability by both theoretical and experimental works. In their work, carbon shell (<1 nm thickness)-coated FeP NPs are supported on a carbon support (FeP/C) by single step heating of polydopamine (PDA)-coated iron oxide with NaH_2PO_2, which exhibited high HER activity comparable to that of FeP/C without the carbon shell (Fig. 8b1). The durability tests for FeP/C with the carbon shell in acid media proved no significant activity loss for up to 10 000 potential cycles, while FeP/C without the carbon shell indicated an increase in overpotential to ~100 mV even after 5000 cycles. Therefore, the role of the carbon shells in protecting FeP NPs from activity loss is clearly demonstrated (Fig. 8b2).[74]

Based on a number of recent studies, single-layer encapsulation of NPs affords excellent activity but less chemical stability. In contrast, a thick carbon shell (>15 layers) may act as a complete protective layer but impede the efficient adsorption of the reactants to the active material, resulting in poor activity.[71,76,114,115,117] Therefore, it is very essential to simultaneously achieve excellent activity and durability for sustainable electrochemical hydrogen production.

Hu *et al.* have attempted to overcome this problem by controlling the carbon shell thickness to balance the HER performance and durability. They fabricated NiMo bimetallic alloy NPs encapsulated by N-doped graphene layers supported on a 3D N-doped porous graphene network (NiMoNPs/3DNG) through a CVD process. As expected, the HER activity and chemical stability of NiMoNPs/3DNG depended on the number of graphene layers, showing that 1–2 and 2–3 graphene layers exhibited better HER activity but poor stability, while 3–5 layers showed slightly lower HER activity but better durability against metal dissolution under acidic conditions for 24 hours (Fig. 8c1–4).[70] Interestingly, the concept of carbon shell protection has been pronounced in abundant studies, regardless of the nature of metal core NPs.[61,71,106,113–115,117,146] However, the core metal/alloy composition is a crucial parameter for the development of highly efficient and durable HER catalysts, which requires deep understanding of physicochemical and electronic properties through experimental and theoretical studies. Several HER stability studies of carbon shell-encapsulated metals/alloys are listed in Table 1.

4.2.2 Oxygen evolution reaction (OER). Compared to the HER catalysts, most of the OER catalysts based on Earth-abundant materials have limited practical applications in water electrolyzers due to their sluggish kinetics (multi-electron transfer and high energy barrier) and poor durability under extremely oxidative environments.[54,65,94,147] Therefore, the development of inexpensive catalysts with high activity and durability remains a challenging aspect. As in HER applications, carbon-encapsulated metal nanostructures show promise as OER catalysts due to their high activity and enhanced chemical stability.[59,65,69,107,109,113,148] However, inevitably, the graphitic carbon shell layers are prone to carbon oxidation/degradation under a more positive potential (>0.2 V *vs.* RHE).[132,149] Therefore, for OER applications, it is very important to design M@C catalysts with an appropriate carbon shell thickness and structure for robust activity and durability.

In view of the above challenges, L. Du *et al.* attempted to synthesize a highly durable N-doped carbon shell encapsulated NiFe OER catalyst through pyrolysis of NiFe-MOFs.[63] The optimized catalyst $Ni^{II}Fe^{III}$@NC had spherical particles shielded by 6–12 carbon layers with a high degree of graphitization (DOG). OER activity of alloyed $Ni^{II}Fe^{III}$@NC and $Ni^{II}Fe^{II}$@NC catalysts with different Ni/Fe ratios is superior in alkaline solution to that of individual counterparts (Fig. 9a1). XANES and EXAFS studies of NiFe@NC spectra reveal that the encapsulated Ni

 This journal is © The Royal Society of Chemistry 2021

Published on 19 2564. Downloaded on 1/2/2569 7:34:44.

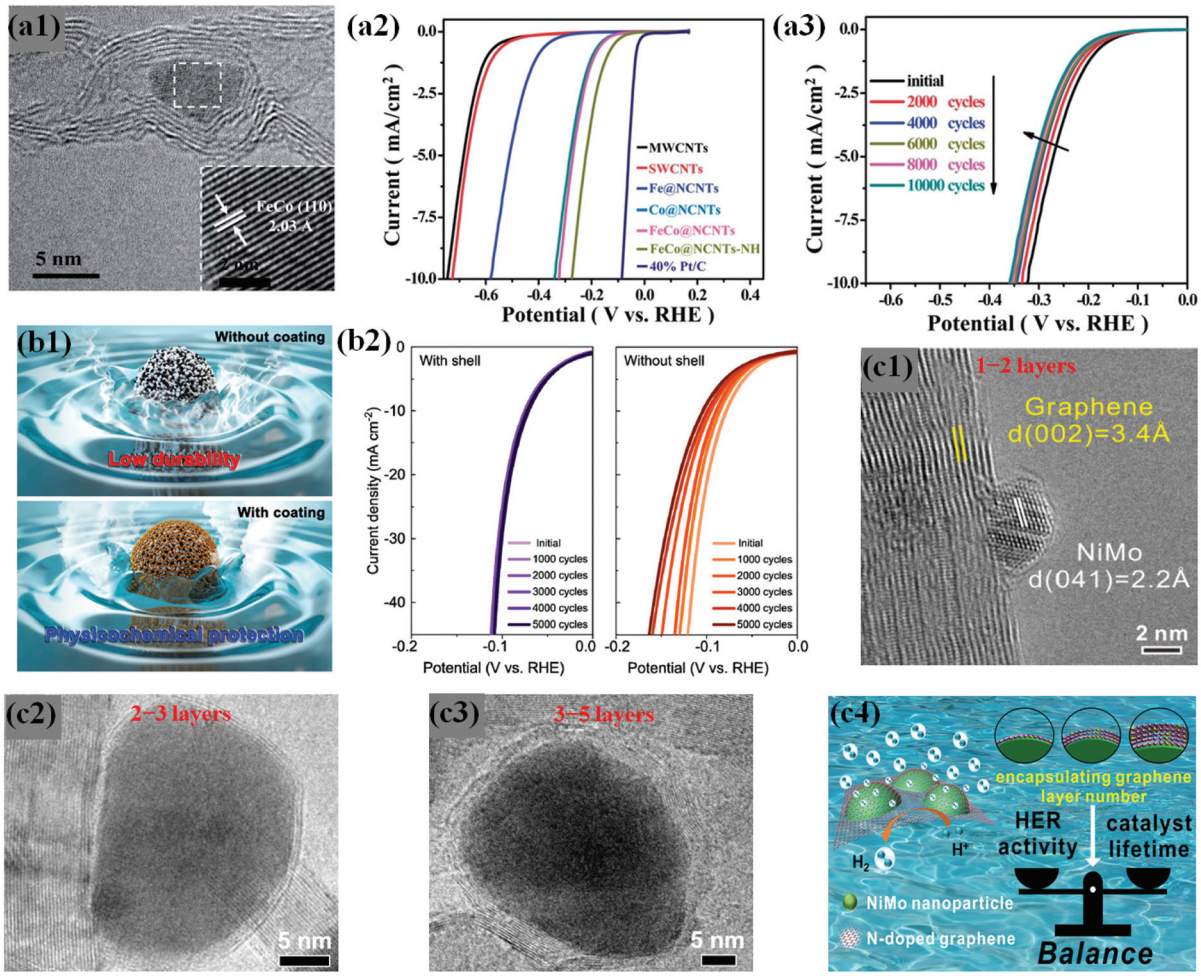

Fig. 8 (a1) HRTEM image of FeCo@NCNTs with the inset showing the (110) crystal plane of the FeCo nanoparticle. (a2) Polarization curves of Fe@NCNTs, Co@NCNTs, FeCo@NCNTs, and FeCo@NCNTs–NH along with MWCNTs, SWCNTs and 40% Pt/C for comparison. (a3) Durability measurement of FeCo@NCNTs: polarization curves recorded initially and after every 2000 CV sweeps between +0.77 and _0.18 V (*vs.* RHE) at 100 mV s^{-1}. All the polarization curves were recorded in 0.1 M H_2SO_4 at a scan rate of 2 mV s^{-1}, reproduced with permission from ref. 59, RSC publications copyright 2014. (b1) Schematic illustrations of FeP NPs with and without carbon shell coating. (b2) Polarization curves for FeP/C with and without a carbon shell and commercial Pt/C electrocatalysts. The corresponding Tafel plots are shown in the inset. Data from control experiments with the samples with no NPs ("C with shell") and iron oxide NPs instead of FeP ("FeOx with shell") are shown together. Electrochemical performance for the HER is measured in 0.5 M H_2SO_4 solution with a rotating ring disk electrode at a rate of 2000 rpm. (b3) Long-term durability test of FeP/C electrocatalysts showing polarization curves for 5000 cycle tests of FeP NPs with (left) and without (right) a carbon shell, adapted with permission from ref. 74, ACS publications, copyright 2017. (c1) Typical HRTEM image of the NiMo NP encapsulated by a monolayer graphene sheet on 3DNG. (c2) High-resolution TEM images of 3DNG supported NiMoNPs encapsulated by 2–3 layers. (c3) High-resolution TEM images of 3DNG supported NiMoNPs encapsulated by 3–5 layers. (c4) Graphics depicting the importance of appropriate carbon shell layers, which provides the balance between HER activity and catalyst lifetime, adapted with permission from ref. 70, ACS publications, copyright 2018.

and Fe have separate roles that boost the activity. Ni was found to tune the local and electronic structure through the strain effect and triggers inert graphite, whereas Fe contributes to electron transfer.

Durability studies under harsh alkaline conditions (1 M KOH) demonstrated that $Ni^{II}Fe^{III}$@NC with a high DOG exhibited robust activity without significant activity loss upon up to 25 000 accelerated degradation test (ADT) cycles between 1.2 and 1.9 (Fig. 9a2). The TEM image of $Ni^{II}Fe^{III}$@NC after the ADT shows no carbon shell corrosion (Fig. 9a3). In contrast, $Ni^{II}Fe^{II}$@NC with a poor DOG shows a significantly decreased activity under the same conditions, indicating severe carbon corrosion (Fig. 9a4).[63] Therefore, the encapsulation strategy using a highly graphitized carbon shell layer is very effective in improving the durability of OER catalysts and provides insights into industrial applications. Similarly, recent studies demonstrated that the carbon shell modified with heteroatom dopants (B, N, P, and S) ensures efficient OER catalysis along with durability.[71,131,147,150]

Nevertheless, the doping level in the carbon shell layer of M@C catalysts should be carefully controlled since there are several factors that balance OER activity and chemical stability.

Published on 19 2564. Downloaded on 1/2/2569 7:34:44.

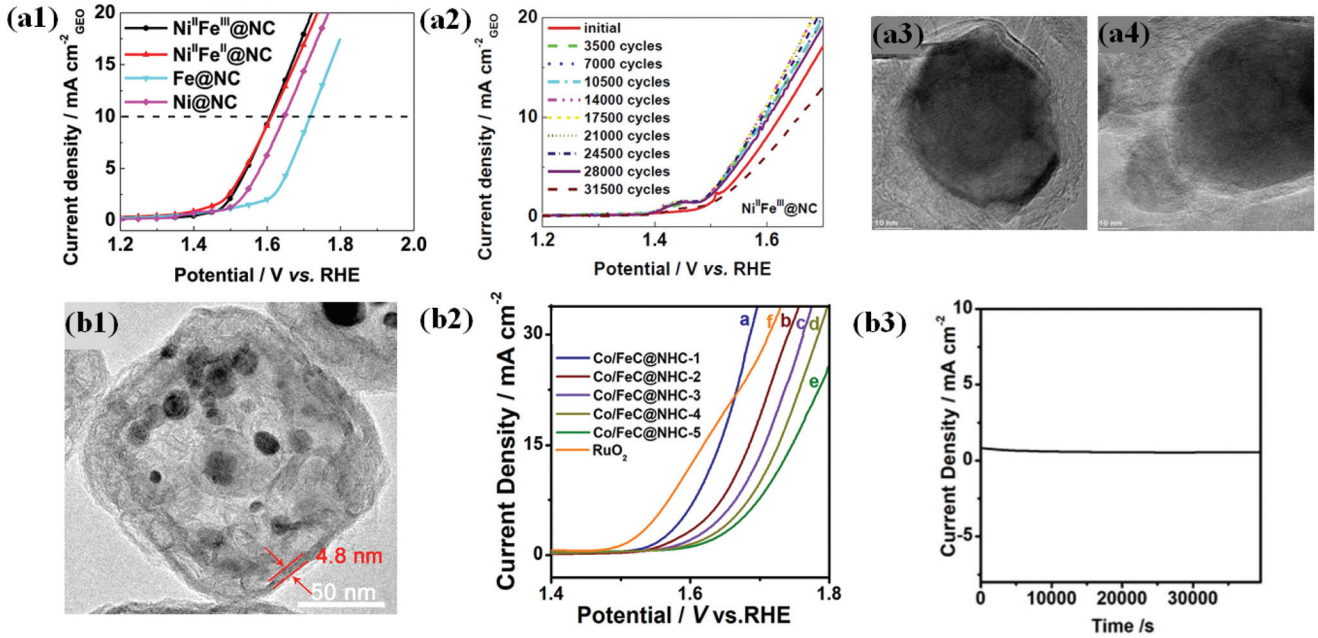

Fig. 9 (a1) LSV curves (10 mV s^{-1}@900 rpm) of $Ni^{II}Fe^{III}$@NC, $Ni^{II}Fe^{II}$@NC, $Fe^{III}_4[Fe^{II}(CN)_6]_3$ derived Fe@NC and $Ni^{II}[Ni^{II}(CN)_4]$ derived Ni@NC catalysts in oxygen-saturated 0.1 M KOH solutions. (a2) LSV curves of $Ni^{II}Fe^{III}$@NC after a certain number of ADT cycles between 1.2 and 1.9 V at 500 mV s^{-1}. TEM images of (a3) $Ni^{II}Fe^{III}$@NC and (a4) $Ni^{II}Fe^{II}$@NC catalysts after ADT, reproduced with permission from ref. 63, Elsevier copyright 2017. (b1) TEM images of (A) Co/FeC@NHC-1 (b2) OER polarization curves of Co/FeC@NHC-1, Co/FeC@NHC-2, Co/FeC@NHC-3, Co/FeC@NHC-4, Co/FeC@NHC-5, and RuO_2 in 1 M KOH. (b3) Potentiostatic response (current density *versus* time) under a constant potential of 1.54 V *vs.* RHE, reproduced with permission from ref. 151, Elsevier copyright 2020.

In another way, Zhang and co-workers proposed the fabrication of highly durable Co/FeC NPs embedded in a cubic N-doped hollow carbon matrix (Co/FeC@NHC) with tunable thickness from the MOF precursor (Fig. 9b1).[151] The OER activity of the Co/FeC@NHC catalyst increased with decreasing the thickness of the carbon matrix (Fig. 9b2). The outstanding durability of Co/FeC@NHC is attributed mainly to the protection of the embedded core Co/FeC NPs by the carbon shell from harsh alkaline environments, showing extremely stable performance during chronoamperometry at a constant potential of 1.54 V *vs.* RHE (Fig. 9b3). However, maintaining high durability under wide pH conditions is still technically challenging. Recently reported OER stability studies of carbon shell-encapsulated metals/alloys are summarized in Table 2.

4.2.3 Oxygen reduction reaction (ORR). Along with OER catalysts for water electrolysis, it is very important to improve the durability of ORR catalysts for fuel cells. Even Pt-based catalysts rapidly lose their activity during a long-term operation due to structural deterioration such as dissolution and agglomeration. Promising catalyst structures such as alloys, Pt-skeleton, Pt-skin, and core–shell have been proposed for decades to reduce the degradation rate of fuel cell catalysts.[135,152–159] However, the durability issues have not been addressed since the active metal surface is still exposed to harsh environments. Therefore, it is necessary to design an ideal catalyst structure that can protect the metal surface by itself while sufficiently opening the active sites.

In this regard, M@C type catalysts encapsulated in carbon shells with appropriate thickness and porosity have been intensively developed. The concept of M@C catalysts can be applied to both noble and non-precious metal-based NPs. As shown in Fig. 10, the TEM image shows the typical morphology of M@C NPs, and the change in the polarization curves before and after ADTs indicates extremely high durability of the M@C catalyst. Regardless of the type of carbon support, carbon-encapsulated Pt- and Pd-based NPs have been mainly investigated.[49,51–53,99,160,161]

For Pt@C type catalysts, Pt@CS/CNF, which is prepared with the N-containing polymer and Pt precursor, exhibited high activity and durability not only under half-cell conditions but also in unit cell tests, satisfying the DOE target of 2025 (voltage loss@0.8 A cm^{-2} <30 mV, ECSA loss <40%) after ADTs using the DOE protocol.[162] In the case of Pt-based alloy catalysts, it is very important to prevent the dissolution of 3d TMs that change the Pt electronic structure by strain and electronic effects. Accordingly, Sung *et al.* synthesized highly durable PtFe NPs with a face-centered-tetragonal (fct) structure through polydopamine (PDA) coating followed by a high-temperature annealing process.[51] The thickness of the carbon shell was rationally controlled by changing the polymer coating time, and the fct–PtFe alloy structure was achieved by using the carbon shell as a hard template during heat treatment. In the half-cell test, the half-wave potential ($E_{1/2}$) of the fct–PtFe/C catalyst decreased by less than 10 mV after ADT (for Pt/C, $E_{1/2}$: decreased by more than 100 mV), exhibiting excellent stability.

 This journal is © The Royal Society of Chemistry 2021

Published on 19 2564. Downloaded on 1/2/2569 7:34:44.

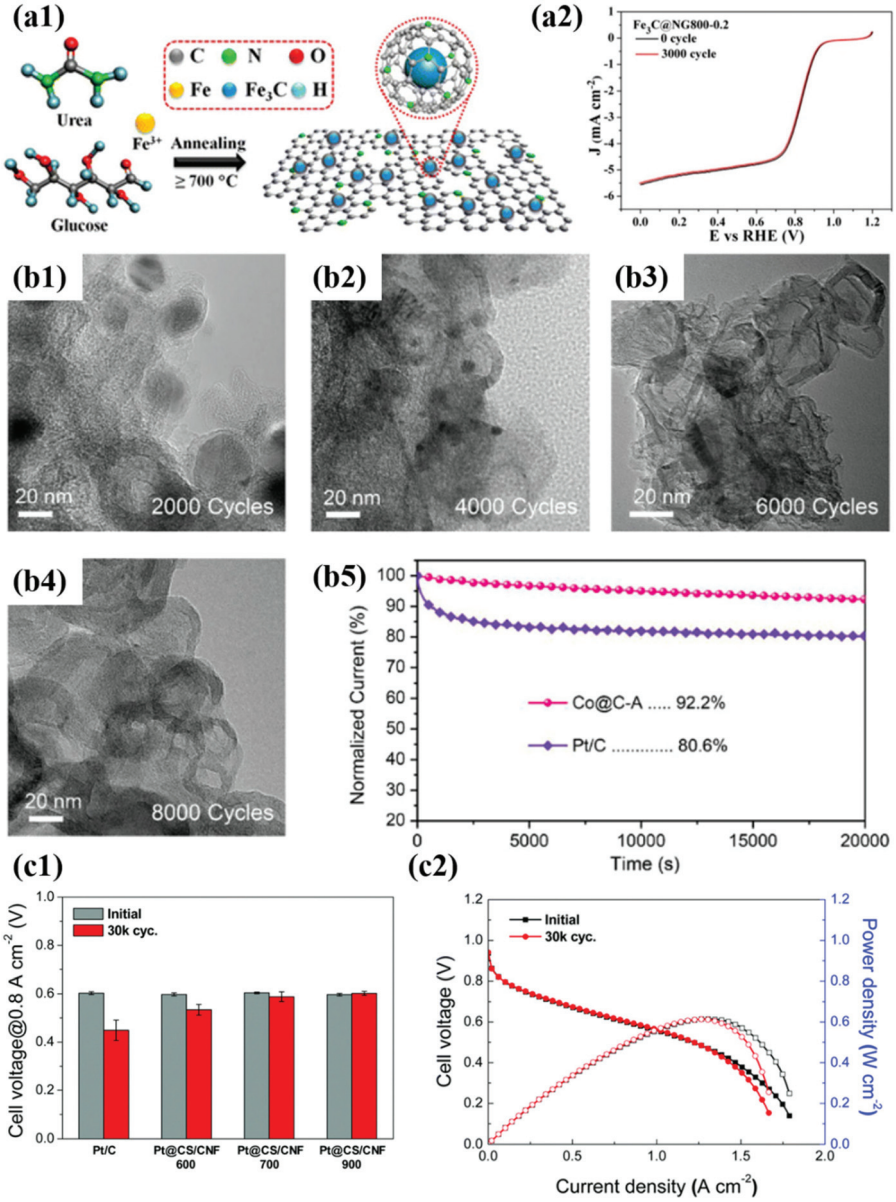

Fig. 10 (a1) Schematic illustration of synthesis of Fe_3C@NG (a2) ORR curves of the Fe_3C@NG800 before and after 3000 cycles in O_2-saturated 0.1 M KOH solution, reproduced with permission from ref. 164, ACS copyright 2015. (b1–4) TEM images of Co@C-A before and after ADT. (b5) Chronoamperometry of Co@C-A for 20 000 s compared to commercial Pt/C in O_2-saturated 0.1 M KOH, reproduced with permission from ref. 97, Wiley copyright 2019. (c1) Cell voltages measured at 0.1 A cm^{-2} of MEAs before and after ADT. (c2) Polarization curves of Pt@CS/CNF900 before and after ADT, reproduced with permission from ref. 162, RSC copyright 2019.

Particularly, in the unit cell test, the maximum power density decreased only by 3.4% (for Pt/C, the maximum power density loss: 27%).

Pd-Based NPs have been extensively studied as ORR catalysts since Pd has an electronic structure similar to Pt. As expected, Pd shows high ORR activity in both acid and alkaline solutions; however, the durability cannot be guaranteed, especially in acidic environments. Therefore, to improve the durability of Pd-based catalysts, Kwon *et al.* proposed N-doped carbon shell-encapsulated Pd NPs (Pd-PANI-K), which are fabricated using aniline as the carbon and nitrogen sources. Wang *et al.* developed Pd-based alloy (PdFe) NPs encapsulated by a graphitic carbon layer *via* a one-step thermal annealing method.[49] In their study, the O–Pd–Fe@NC/C catalyst annealed at 800 °C showed 74.5% MA and 57.2% SA losses after 10 000 cycles in an acid solution, while Pt/C indicated a loss in MA of 83.8% and SA of 88.2% under the same conditions. In particular, in alkaline solution, $E_{1/2}$ of the O–Pd–Fe@NC/C catalyst decreased by only 2 mV even after 30 000 cycles.

Recently, non-precious metal-based catalysts such as Fe- and Co-based materials have attracted much more attention to

Published on 19 2564. Downloaded on 1/2/2569 7:34:44.

replace Pt- and Pd-based catalysts. Although carbon-encapsulated TM NPs have been reported since 2000,[47,97,163–165] in contrast to precious metal catalysts, both catalytic activity and durability issues remain challenging. For instance, N-doped graphene-supported Fe_3C@C showed a negligible decrease in $E_{1/2}$ after 3000 cycles in O_2 saturated 0.1 M KOH.[75] However, the number of potential cycles for ADT was not sufficient to evaluate the protective effect of the carbon shell.[164] However, a few studies on Co-based catalysts such as Co_9C_8@C and Co@C-MOF adopted harsh test conditions with 5000–8000 potential cycles in alkaline solution, showing much enhanced durability compared to Pt/C.[163,164] However, Co-based NPs still suffered from metal dissolution and detachment from carbon supports during the ADTs.

In contrast, Yoo *et al.* suggested highly stable Co@C/C catalysts synthesized by a bottom-up approach to the carbon shell formation.[47] In this fabrication method, the Co precursor containing acetylacetonates as carbon sources is thermally decomposed and then provides the carbon atoms to reduced Co NPs. The carbons incorporated into the Co NPs are diffused to the metal surface and simultaneously graphitized during a high-temperature annealing process, forming a robust thin carbon shell (less than 1 nm) at the sub-nm level. The ORR activity of the synthesized Co@C/C catalyst hardly changed even after 5000 potential cycles, exhibiting extremely high durability compared to Pt/C. In addition, the Co@C NPs maintained the initial structure even after the ADTs due to the protective effect of the graphitic carbon shell. Therefore, it is believed that the interfacial bonding strength between the carbon shell and the core metal NP can be affected by the fabrication method. Nevertheless, it is necessary to develop non-precious metal-based M@C catalysts that exhibit high stability under both acid and alkaline conditions.

4.2.4 Hydrogen oxidation reaction (HOR). In recent years, Jung *et al.* reported the development of Pt@C/C catalysts for the HOR, and compared the electrochemical properties of Pt@C/C catalysts with different carbon shell structures, which were annealed at 600 and 900 °C.[80] As a result, the carbon shell graphitized at a higher temperature has much improved stability due to enhanced crystallinity. Even after 3000 potential cycles in an acid solution, the HOR performance and structure of the Pt@C/C catalyst hardly changed. In particular, the carbon shell-encapsulated Pt NPs maintained a particle size of ~3 nm, and the carbon shell layers were clearly identified after the ADTs.

In addition, Gao *et al.* synthesized Ni@C NPs as non-precious metal-based catalysts by heat treatment at 500, 600, and 700 °C, respectively (Fig. 11).[56] Despite the low HOR activity, after 10 000 cycles in alkaline solutions, Ni@C catalysts showed negligible performance degradation, as follows: 20% (500 °C), 8% (600 °C), and 0% (700 °C), respectively. From the XPS analysis, it was confirmed that the number of C–C bonds increases and the interaction between the metallic Ni NP and the carbon shell becomes stronger as the annealing temperature increases. In addition, the enhanced crystallinity of the carbon shell was clearly identified by Raman spectra showing the change in the D/G ratio.[80] Unfortunately, few studies have been conducted on M@C catalysts for the HOR; however, in contrast, it can be thought that there is plenty of room for new research.

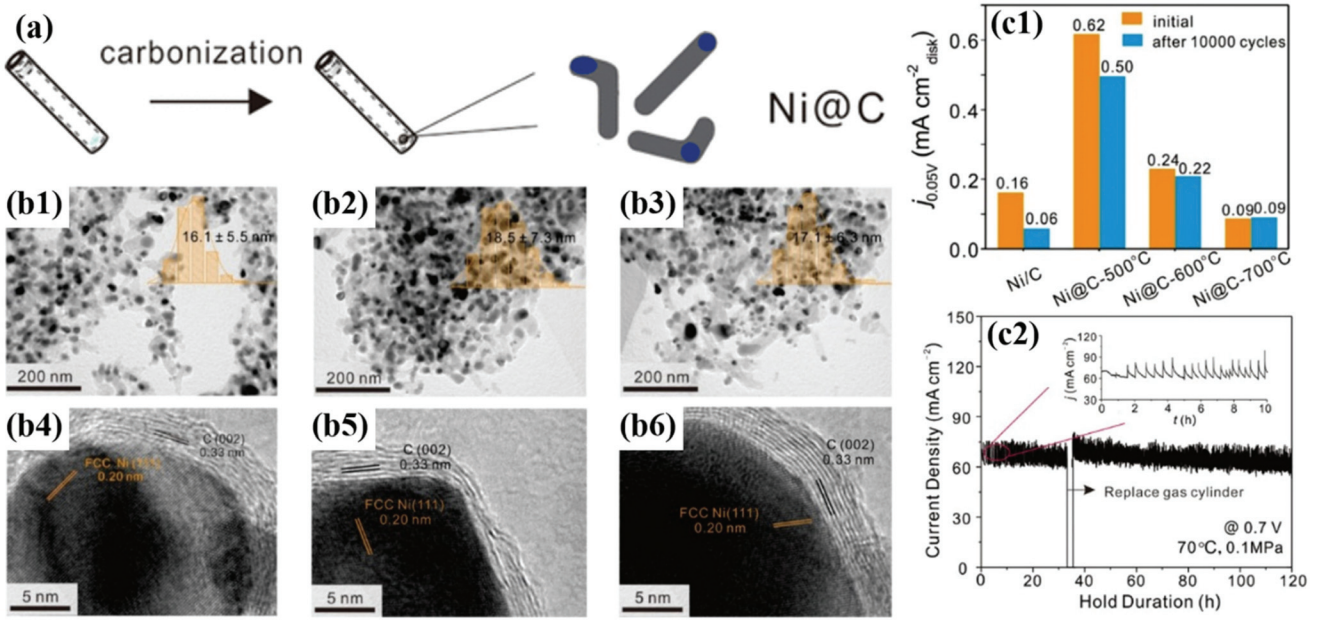

Fig. 11 (a) Synthesis diagram of the Ni@C catalyst. (b1–3) TEM images of Ni@C with the inset showing the particle sized distribution histogram. (b1–6) HR-TEM images of Ni@C showing carbon shell thickness for Ni@C-500, Ni@C-600, and Ni@C-700, respectively. (c1) Current densities of Ni@C catalysts before and after ADT (10 000 cycles). (c2) Stability test at 0.7 V for 120 h under single cell conditions at 70 °C with fully humidified H_2 and O_2 fed at the anode and cathode, respectively, with permission from ref. 56, ACS copyright 2020.

This journal is © The Royal Society of Chemistry 2021

Published on 19 2564. Downloaded on 1/2/2569 7:34:44.

4.2.5 Multifunctional catalysts for hydrogen and oxygen reactions. The development of electrocatalysts with multifunctional ability to catalyse various electrochemical processes such as the HER/OER, ORR/OER, and HER/OER/ORR is currently a hot research topic and has great potential for commercial values, since multifunctional electrocatalysts can reduce the overall cost of the electrochemical setup and make the system easier for future energy conversion and energy-storage applications (Fig. 12a).[72,91,133,166–168] Unfortunately, to date, multifunctional catalysts with high efficiency suitable under wide pH conditions are still not developed. Noble metal-based catalysts such as Pt or Pd show high activity for the ORR and HER, while OER active catalysts such as RuO_2 or IrO_2 were inactive for the ORR and HER. In particular, these noble metal catalysts show an inability to accelerate ORR and OER processes simultaneously and exhibit poor bifunctional activity.[169,170]

However, in recent years, numerous efforts have been devoted to the development of novel metal encapsulated carbon shell materials as promising multifunctional or bifunctional electrocatalysts because the concept of metal–carbon hybrid interaction and their electronic structure modification are expected to manifest multifunctional activity.[54,94,119,127,171–173] In particular, first-row TMs (Mn, Co, Ni, and Fe) and their alloys have been well explored due to their improved intrinsic activity by electronic modification of enveloping carbon layers. Importantly, metal alloy-based catalysts such as FeCo, NiCo, and FeNi exhibit superior bifunctional or multifunctional activity to their individual counter-

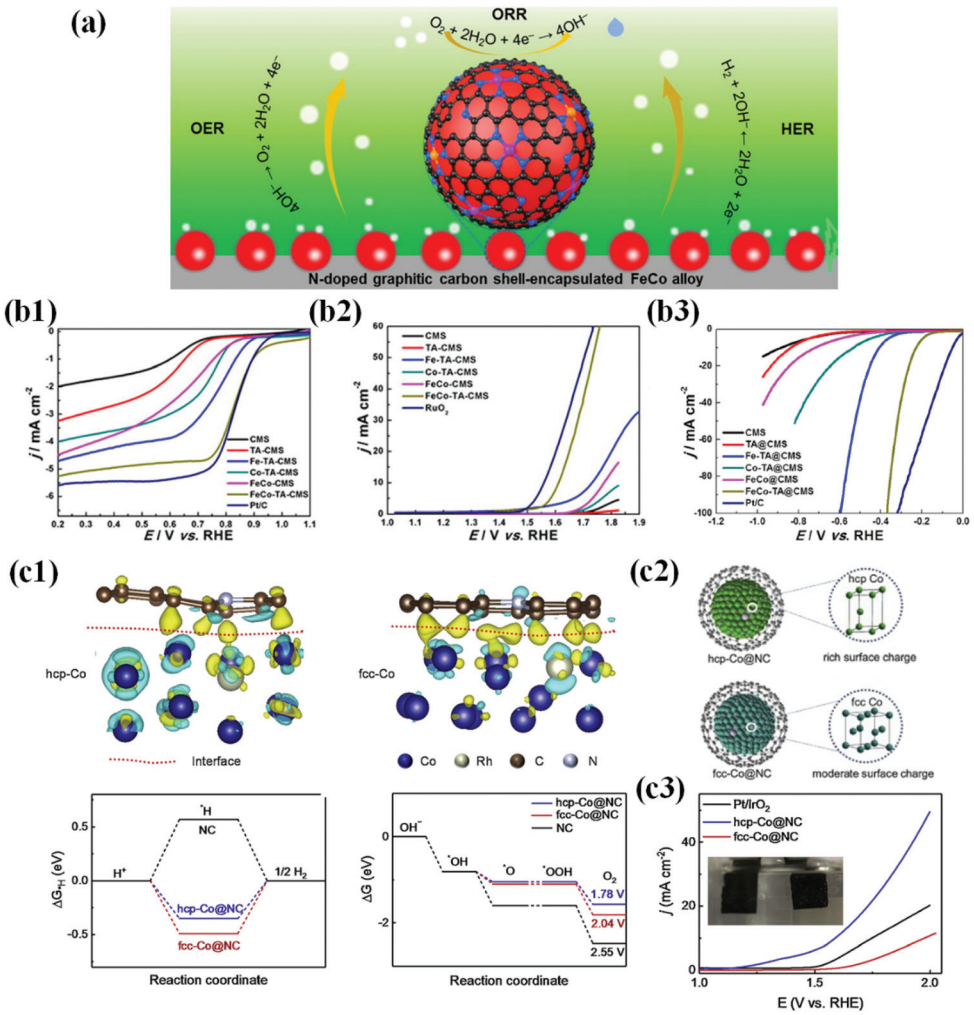

Fig. 12 (a) Multifunctional activity of the N-doped carbon shell coated FeCo alloy for the ORR, OER and HER. (b1) Electrocatalytic performances of all as-prepared catalysts and Pt/C for the ORR. LSV curves and the corresponding half wave potential ($E_{1/2}$) of FeCo-TA@CMS, FeCo@CMS, Fe-TA@CMS, Co-TA@CMS, TA@CMS, CMS, and Pt/C in O_2-saturated 0.1 M KOH at room temperature. (b2) LSV curves of FeCo-TA@CMS, FeCo@CMS, Fe-TA@CMS, Co-TA@CMS, TA@CMS, CMS, and RuO_2. (b3) LSV curves of FeCo-TA@CMS, FeCo@CMS, Fe-TA@CMS, Co-TA@CMS, TA@CMS, CMS and Pt/C, reproduced with permission from ref. 91, Elsevier publications, copyright 2021. (c1) TEM micrographs of G-$Co_{0.5}Fe_{0.5}$ (before and after electrochemical activation. (c2) Electrochemical OER activities of graphite-encapsulated 3d TMs and their alloys in 1 M KOH solution scanned at 10 mV s^{-1}. (c3) Electrochemical HER activities of graphite-encapsulated 3d TMs and their alloys in 0.1 M KOH solution scanned at 10 mV s^{-1}, reproduced with permission from ref. 177, Elsevier publications, copyright 2020.

Published on 19 2564. Downloaded on 1/2/2569 7:34:44.

parts since the meta-metal bonding enhances intrinsic polarity and facilitates charge transfer.[59,113,174,175] Liu *et al.* proposed the multifunctional ability of FeCo alloy NPs encapsulated in the N-doped carbon shell prepared by a simple pyrolysis process and identified that the FeCo catalysts exhibit superior activity to individual metal species for the ORR, OER, and HER (Fig. 12b1–3).[91]

Recently, Goodenough and co-workers developed a series of trifunctional electrocatalysts based on binary and ternary alloys of Fe, Co, and Ni NPs encapsulated by graphitic carbon shells. The initially synthesized catalysts had a thick graphitic shell (~20–30 layers) that was not catalytically active due to the suppression of charge penetration efficiency. However, this situation is circumvented when the catalysts undergo electrochemical exfoliation through the surface activation process by potential cycling between 1.2 and 2.0 V *vs.* RHE in an alkaline solution. Consequently, this electrochemical exfoliation transformed the inert thick graphite layer into a thin, highly active graphene shell (1–3 layers). Screening of the activated catalysts for the ORR, OER, and HER in alkaline solutions indicated that the binary Ni–Fe system showed the best activity for the OER, and the Co–Fe system was promising for the HER and ORR.[176] As the catalytic reactions occur on the surface, the strong metal–carbon electronic interactions at the interface are significant to tailor the surface charge density and to improve physicochemical properties of the outer carbon shell towards their multifunctional characteristics. However, this depends on the electronic properties and charge injection capability of metal/alloy cores.[72,86,119] For instance, Li *et al.* demonstrated that the hcp-Co@NC catalyst composed of hcp-Co NPs encapsulated by the N-doped carbon shell triggers delocalization of interfacial charge density and strong electronic coupling at the interface, while the fcc-Co@NC catalyst is not possible. Consequently, when hcp-Co@NC NPs are applied to a water electrolyzer, superior reaction activity and good stability are realized, requiring only 1.58 V to attain 10 mA cm^{-2} (Fig. 12c).[177] Interestingly, it was reported that tuning of metal/alloy composition can also have a strong influence on the electronic structure of graphene shells, tailoring the catalytic activity.[178]

Several factors such as appropriate metal composition, carbon shell thickness, and dopant level can affect the multifunctional performance of M@C type catalysts. According to the design of the catalyst structure, the activity and durability can be dramatically modulated. This scenario was exemplified by Noh *et al.* when they fabricated a series of TM alloys encapsulated in an N-doped carbon shell (M@N–C, M = Fe, Co, Ni, Cu, or Fe alloys) supported on Ketjen black (KB) as bifunctional electrocatalysts. Based on the screening result of different transition metals, FeCo@N–C/KB was found to achieve excellent bifunctional activity toward the HER as well as ORR with high durability in acidic solutions. By DFT and experimental investigations on the number of factors (N-doping level, active N sites, thickness of shell layers, and alloying elements), a quantitative method is proposed to tune the ORR activity by carefully controlling the aforementioned factors (Fig. 13a1–3).[179]

Recently, Li *et al.* developed an efficient bifunctional electrocatalyst composed of FeCo alloy NPs coated by an ultrathin N-doped carbon layer (~1–3) encapsulated in N-doped carbon nanotubes (FeCo@NC/NCNTs) (Fig. 13b1). Electrochemical measurements show that the optimized catalyst, $Fe_{1.2}$Co@NC/NCNTs, with a low Fe/Co content exhibits high ORR activity, while OER activity of the same exhibited superior activity among all the catalysts in an alkaline medium. The potential difference ($\Delta E = E_{j\,=\,10} - E_{1/2}$) between the ORR and OER for $Fe_{1.2}$Co@NC/NCNTs is 0.765 V (Fig. 13b2), which was lower than that of Pt/C and Ir/C. The outstanding ORR and OER activity of the catalyst was found to be due to the following reasons: (1) synergy between Fe and Co in the metal alloy, (2) electronic interaction between FeCo NPs and the N-doped carbon layer, (3) formation of Fe–N_x and Co–N_x bonds generated more active sites for the OER, and (4) enhanced conductivity.[58] The potential difference (ΔE) as an important descriptor of bifunctional (ORR/OER) activity can be further manipulated by tuning the metal composition ratios (Fig. 13b3).[54]

In addition, co-doping other heteroatoms (B, S, and P) with nitrogen in graphene is proven to potentially improve bifunctional activity as well.[179–181] Zhang *et al.* studied bifunctional water splitting reactions on Co encapsulated B/N co-doped nanocarbon by carbonization of the Co-MOF precursor. The optimized catalyst, Co/NBC-900, in their work displayed efficient bifunctional activity and stability toward the HER and OER in alkaline media.[182]

In some instances, coupling two different metal species to form an alloy alters the lattice and bond length of the crystals and changes the adsorption energies of reactive intermediates for optimal catalytic activity toward bifunctional or multifunctional electrocatalytic activity.[76,183] For instance, incorporating Mo into bimetallic NiFe-based catalysts may emerge as a new type of ternary metal electrocatalyst and can potentially serve as bifunctional electrocatalysts toward the overall water splitting process owing to improved metal–hydrogen (M–H) strength and enhanced affinity toward OH^- ions.[184–186] Hu *et al.* in their work demonstrated the above concept by doping MoC_2 in NiFe NPs encapsulated in N-doped graphene layers (~3–11 layers) for water electrolysis. The electrochemical tests and structural analysis proved that the MoC_2-doped NiFe cores were the active sites for the HER/OER but not the N-doped carbon shell (Fig. 13c1 and 2), which took the role to provide high conductivity and chemical protection against corrosion/oxidation during long-term durability tests. However, OER stability tests indicated inevitable *in situ* formed oxidized species (*i.e.*, Ni^{2+}, Fe^{2+}, and Mo^{3+}), which acted as additional active sites for the OER (Fig. 13c3).[72]

4.3 Reaction-selective catalysts *via* fine-control of the carbon shell structure

First of all, we introduce the development of alcohol-tolerant M@C catalysts for the ORR in fuel cells.[49,50,75,187,188] Direct alcohol fuel cells (DAFCs) have been extensively studied due to their high energy density and safety of fuel storage. In DAFCs, along with the alcohol oxidation reaction (AOR) at the anode,

 This journal is © The Royal Society of Chemistry 2021

Published on 19 2564. Downloaded on 1/2/2569 7:34:44.

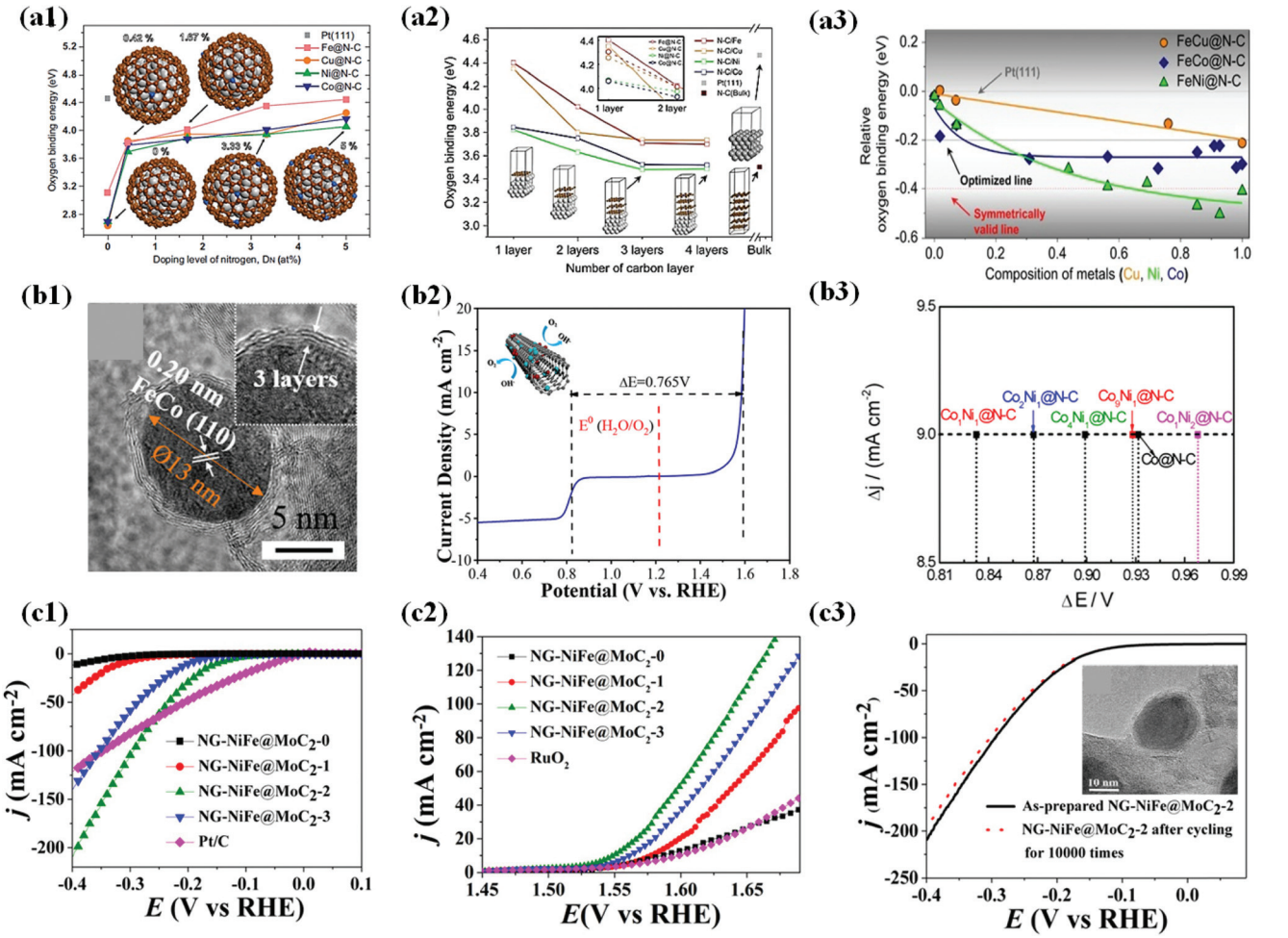

Fig. 13 (a1) Oxygen binding energies as a function of the doping level of nitrogen on M@N–C (M = Fe, Cu, Ni and Co) as a function of DN, typically 0, 0.42, 1.67, 3.33 and 5 at%. The oxygen binding energy (4.46 eV) on Pt(111) is marked for comparison with those on M@N–C. (a2) Oxygen binding energy as a function of the number of carbon layers for N–C/M (bulk) and M@N–C (nanoparticle, 1.5 nm) as a function of the number of carbon layers, including Pt(111) and N–C (bulk). (a3) Relative oxygen binding energies on FeM@N–C NPs as a function of the composition of second metal (M). Oxygen binding energies are represented as E(FeM@N–C) E(Pt(111)), where E(FeM@N–C) and E(Pt(111) are oxygen binding energies on FeM@N–C and Pt(111), respectively, reproduced with permission from ref. 179, Nature group publications, copyright 2019. (b1) HRTEM images of the $Fe_{1.2}Co$@NC/NCNTs. (b2) Overall polarization curve of the $Fe_{1.2}Co$@NC/NCNTs in the entire ORR and OER region, reproduced with permission from ref. 58, ACS publications, copyright 2018. (b3) Potential differences ($E_{@6.0\ mA\ cm^{-2}} - E_{@-3.0\ mA\ cm^{-2}}$) on Co_xNi_y@N–C, reproduced with permission from ref. 54, ACS publications, copyright 2018. (c1) Steady-state polarization curves of NGNiFe@MoC_2-0, NG-NiFe@MoC_2-1, NGNiFe@MoC_2-2, NG-NiFe@MoC_2-3 and Pt/C electrocatalysts for HER. (c2) Steady-state polarization curves of NGNiFe@MoC_2-0, NG-NiFe@MoC_2-1, NGNiFe@MoC_2-2, NG-NiFe@MoC_2-3 and RuO_2 electrocatalysts for OER. (c3) HER polarization of NG-NiFe@MoC_2-2 before and after cycling for 10 000 times. Inset shows HRTEM image of NG-NiFe@MoC_2-2 after 10 000 cycles, reproduced with permission from ref. 72, Elsevier publications, copyright 2018.

the sluggish ORR kinetics at the cathode is a crucial factor in decreasing fuel cell performance. In addition, it is well known that the alcohol crossover from the anode to the cathode impedes the ORR by forming a mixed potential, causing serious performance degradation. Accordingly, in the past decades, to improve the cathode performance, Pt-based alloys NPs such as PtPdCo have been developed as alcohol-tolerant cathode catalysts.[189] However, it is very difficult to completely prevent the formation of a mixed potential since the surface of metal alloy NPs is still exposed to the crossovered alcohols.[189]

Accordingly, Wang *et al.* demonstrated that a thick carbon shell perfectly encapsulating the PdFe alloy surface can significantly reduce the alcohol crossover effect.[50] As shown in Fig. 14a, the CV and ORR polarization curves of the O–Pd–Fe@NC/C catalyst hardly changed even after injecting 0.5 M methanol into the electrolyte, resulting in much enhanced alcohol tolerance compared to Pt/C. In addition, the Fe/Fe_3C@C catalyst maintained the ORR current for 1000 s after adding the methanol solution to both acidic and alkaline solutions (Fig. 14a).[188] Cheng *et al.* also encapsulated Pt NPs in a 3D-structured N-doped carbon nanocage (Pt@NCNC) through a vacuum filling process, showing high methanol tolerance without change in ORR activity.[187] Therefore, it is clearly confirmed that the blocking effect by the carbon shell coated on

Published on 19 2564. Downloaded on 1/2/2569 7:34:44.

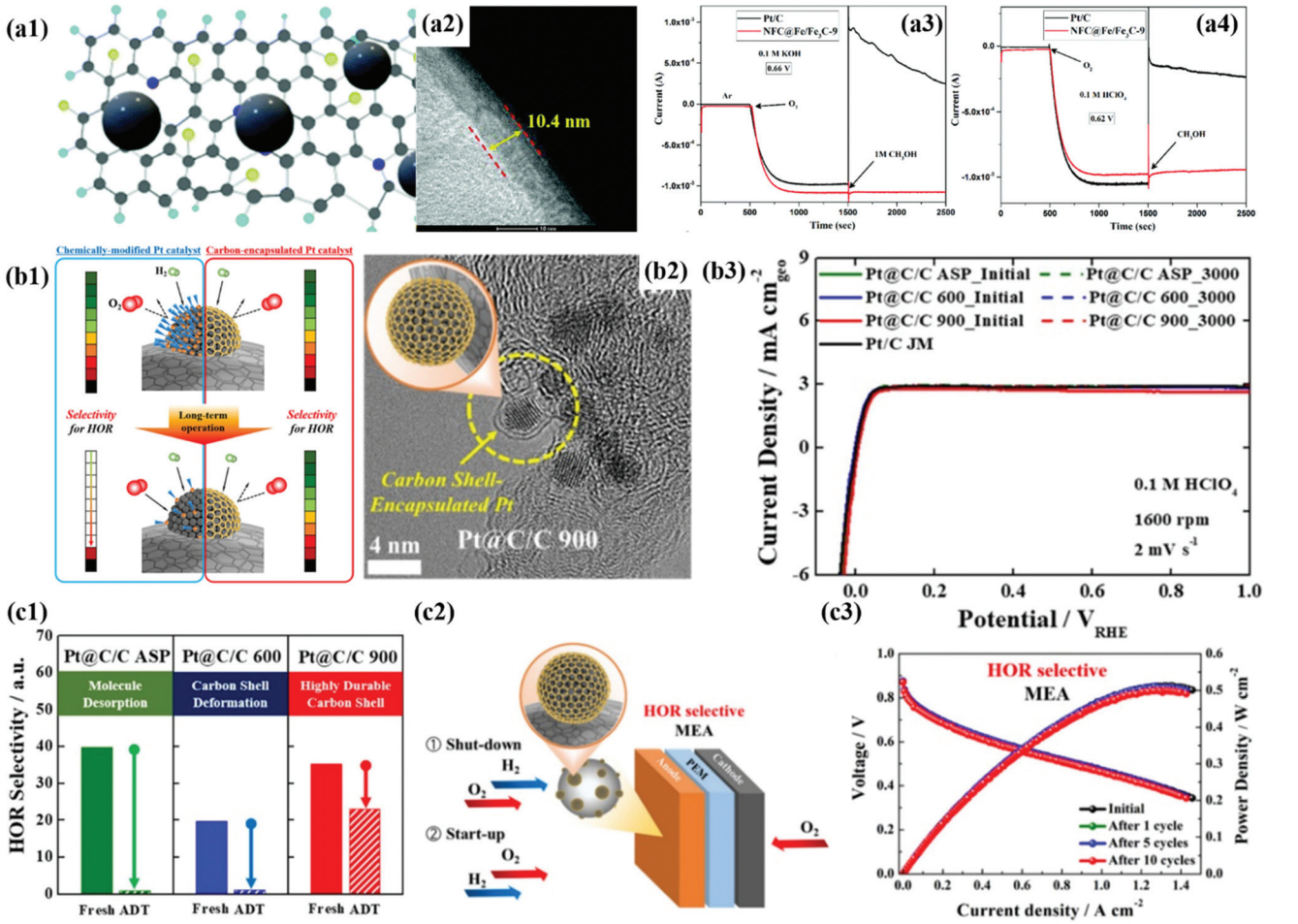

Fig. 14 (a1) Schematic illustration of N and F co-doped carbon (NFC) encapsulated Fe/Fe_3C. (a2) HR-TEM images of NFC@Fe/Fe_3C-9 showing carbon shell thickness. (a3–4) Chronoamperometry of NFC@Fe/Fe_3C-9 for methanol tolerance 0.1 M KOH (a3) and 0.1 M $HClO_4$ (a4), with permission from ref. 75, RSC copyright 2020. (b1) Schematic illustration of HOR selectivity change of the Pt catalyst and carbon encapsulated Pt catalyst during PEMFC operation. (b2) TEM images of Pt@C/C 900 (b3) HOR polarization curves of Pt@C/C catalysts before and after 3000 cycles (b4) exposed Pt surface areas of Pt@C/C catalysts before and after 3000 cycles. (b5) Schematic diagram of the start-up/shut-down cycle test of the single cell system using Pt@C/C catalysts. (b6) *i*–*V* polarization curves of Pt@C/C catalysts during the start-up/shut-down test in the single cell system, with permission from ref. 80, ACS copyright 2019.

the metal NPs is superior to the electronic effect by simple metal alloying. However, to guarantee high ORR activity, it is necessary to develop an alcohol-tolerant M@C type catalyst with a carbon shell that has an appropriate thickness and pores.

Second, during fuel cell operation, a reverse current can occur by the undesired ORR due to the formation of H_2/O_2 boundaries at the anode under shut-down/start-up conditions.[80] It is well known that the reverse current causes serious deterioration of fuel cell performance since a potential of ~1.5 V or higher is applied to the cathode, resulting in catalyst dissolution and carbon corrosion. To avoid this problem, Yoo *et al.* fabricated a Pt@C/C anode catalyst that has high HOR selectivity along with fully subdued ORR activity when H_2/O_2 boundaries are formed in the anode under shut-down/start-up conditions. The finely-tuned carbon shell as a molecular sieve layer rationally induced the selective adsorption/reaction of H_2 rather than O_2 due to the different kinetic diameters of the gases. In particular, the Pt@C/C catalyst heat-treated at 900 °C had a robust carbon shell with high HOR selectivity and exhibited superior chemical stability compared to the catalyst annealed at 600 °C. In unit cell tests, the membrane electrode assembly (MEA) with a HOR-selective anode catalyst showed excellent durability even after shut-down/start-up cycles, while the performance of MEA with a typical Pt/C catalyst significantly decreased (50% reduction) due to serious deterioration of the cathode catalyst layer. Similarly, Choi *et al.* synthesized Pt@C/C catalysts with hydrogen peroxide (H_2O_2) production selectivity against the ORR by controlled coating of Pt NPs, effectively suppressing the 4-electron pathway in the course of the ORR. The carbon shell induced the end-on adsorption of O_2 on the Pt surface, remarkably enhancing the H_2O_2 selectivity up to 41%.[60] Therefore, the M@C type catalyst with reaction selectivity is expected to be a key material that

 This journal is © The Royal Society of Chemistry 2021

Published on 19 2564. Downloaded on 1/2/2569 7:34:44.

can be applied not only to fuel cells, but also to various electrochemical energy conversion reactions.

5. Summary and outlook

Carbon-encapsulated metal (M@C) type catalysts have been extensively studied as promising electrocatalysts for fuel cell and water electrolysis reactions. In this review, we introduced the M@C NPs composed of Earth-abundant TMs and noble metals that can promote the advancement of energy conversion technologies and bridge the gap to the development of energy storage technologies. In particular, the technical achievements by the development of M@C type catalysts trigger the electrocatalytic reactions of the inert carbon shell, ensure the durability of the active material, and facilitate the selective electrochemical reactions by tuning the electronic structure and physicochemical properties of the carbon shell. Furthermore, the N-dopant induces excellent properties of the carbon shell through the modification of the electronic structure and the chemical bonding character between the metal and the outer N-doped carbon than other dopants (B, S, and P). Now, beyond the experimental studies of water electrolysis and fuel cells, an in-depth theory must be established to fully understand interesting phenomena in electrochemical reactions. In particular, in water electrolysis, it is necessary to rationally describe the physical changes of metal NPs encapsulated by the carbon shell during the reaction, and to clearly investigate the role of the carbon shell. Further advances in computational modelling will provide insight into the novel design of M@C type catalysts. Nevertheless, simple and reliable experimental strategies to fabricate a well-defined and fine-tuned carbon shell are always essential to realizing potential applications that will mark great breakthroughs in this field.

Author contributions

S. J. Yoo and N. Jung conceived the idea of the work. J.-H. Jang and A. Anto Jeffry wrote the manuscript. J. Min investigated the paper and research trends. N. Jung and S. J. Yoo guided the work and revised the manuscript.

Conflicts of interest

There are no conflicts to declare.

Acknowledgements

This work was supported by the KIST Institutional Program (2E31002) and a National Research Foundation of Korea (NRF) grant funded by the Korean government (MSIP) (No. 2021R1A2C2012685, 2018M1A2A2061975, and 2021M3H4A1A02042948). This work was also supported by the New & Renewable Energy Core Technology Program of KETEP (20203020030010) in Korea.

Notes and references

1 R. O'hayre, S.-W. Cha, W. Colella and F. B. Prinz, *Fuel cell fundamentals*, John Wiley & Sons, 2016.
2 H. A. Gasteiger and N. M. Marković, *Science*, 2009, **324**, 48–49.
3 O. Z. Sharaf and M. F. Orhan, *Renewable Sustainable Energy Rev.*, 2014, **32**, 810–853.
4 Y. Wang, K. S. Chen, J. Mishler, S. C. Cho and X. C. Adroher, *Appl. Energy*, 2011, **88**, 981–1007.
5 G. Shen, J. Liu, H. B. Wu, P. Xu, F. Liu, C. Tongsh, K. Jiao, J. Li, M. Liu and M. Cai, *Nat. Commun.*, 2020, **11**, 1–10.
6 J. Yang, S. Yang, Y. Chung and Y. Kwon, *Korean J. Chem. Eng.*, 2020, **37**, 176–183.
7 S. Miyanishi and T. Yamaguchi, *Polym. Chem.*, 2020, **11**, 3812–3820.
8 J.-H. Wee, *Renewable Sustainable Energy Rev.*, 2007, **11**, 1720–1738.
9 S. Khilari, S. Pandit, M. Ghangrekar, D. Das and D. Pradhan, *RSC Adv.*, 2013, **3**, 7902–7911.
10 J.-J. Hwang, *Renewable Sustainable Energy Rev.*, 2013, **19**, 220–229.
11 C. Tang, H.-F. Wang and Q. Zhang, *Acc. Chem. Res.*, 2018, **51**(4), 881–889.
12 C. M. Zalitis, D. Kramer and A. R. Kucernak, *Phys. Chem. Chem. Phys.*, 2013, **15**, 4329–4340.
13 A. Roy, M. R. Talarposhti, S. J. Normile, I. V. Zenyuk, V. De Andrade, K. Artyushkova, A. Serov and P. Atanassov, *Sustainable Energy Fuels*, 2018, **2**, 2268–2275.
14 E. Antolini, *Energy Environ. Sci.*, 2009, **2**, 915–931.
15 B. P. Setzler, Z. Zhuang, J. A. Wittkopf and Y. Yan, *Nat. Nanotechnol.*, 2016, **11**, 1020–1025.
16 K. Karthick, A. B. M. Basha, A. Sivakumaran and S. Kundu, *Catal. Sci. Technol.*, 2020, **10**, 3681–3693.
17 Y. P. Zhu, T. Y. Ma, M. Jaroniec and S. Z. Qiao, *Angew. Chem., Int. Ed.*, 2017, **56**, 1324–1328.
18 P. Ganesan, A. Sivanantham and S. Shanmugam, *J. Mater. Chem. A*, 2016, **4**, 16394–16402.
19 N. Armaroli and V. Balzani, *ChemSusChem*, 2011, **4**, 21–36.
20 M. Conte, A. Iacobazzi, M. Ronchetti and R. Vellone, *J. Power Sources*, 2001, **100**, 171–187.
21 V. Das, S. Padmanaban, K. Venkitusamy, R. Selvamuthukumaran, F. Blaabjerg and P. Siano, *Renewable Sustainable Energy Rev.*, 2017, **73**, 10–18.
22 M. Ehsani, Y. Gao, S. Longo and K. Ebrahimi, *Modern electric, hybrid electric, and fuel cell vehicles*, CRC press, 2018.
23 J. M. Ogden, M. M. Steinbugler and T. G. Kreutz, *J. Power Sources*, 1999, **79**, 143–168.
24 R. Van den Hoed, *J. Cleaner Prod.*, 2007, **15**, 1014–1021.
25 Y. Chen, A. Lavacchi, H. Miller, M. Bevilacqua, J. Filippi, M. Innocenti, A. Marchionni, W. Oberhauser, L. Wang and F. Vizza, *Nat. Commun.*, 2014, **5**, 1–6.

Published on 19 2564. Downloaded on 1/2/2569 7:34:44.

26 H. A. Miller, K. Bouzek, J. Hnat, S. Loos, C. I. Bernäcker, T. Weißgärber, L. Röntzsch and J. Meier-Haack, *Sustainable Energy Fuels*, 2020, **4**, 2114–2133.
27 S. Park, Y. Shao, J. Liu and Y. Wang, *Energy Environ. Sci.*, 2012, **5**, 9331–9344.
28 L. Xiao, S. Zhang, J. Pan, C. Yang, M. He, L. Zhuang and J. Lu, *Energy Environ. Sci.*, 2012, **5**, 7869–7871.
29 O. Schmidt, A. Gambhir, I. Staffell, A. Hawkes, J. Nelson and S. Few, *Int. J. Hydrogen Energy*, 2017, **42**, 30470–30492.
30 T. Schuler, T. Kimura, T. J. Schmidt and F. N. Büchi, *Energy Environ. Sci.*, 2020, **13**, 2153–2166.
31 T. Asset, R. Chattot, M. Fontana, B. Mercier-Guyon, N. Job, L. Dubau and F. Maillard, *ChemPhysChem*, 2018, **19**, 1552–1567.
32 N. Jung, D. Y. Chung, J. Ryu, S. J. Yoo and Y.-E. Sung, *Nano Today*, 2014, **9**, 433–456.
33 A. Oh, Y. J. Sa, H. Hwang, H. Baik, J. Kim, B. Kim, S. H. Joo and K. Lee, *Nanoscale*, 2016, **8**, 16379–16386.
34 Q. Shi, C. Zhu, D. Du and Y. Lin, *Chem. Soc. Rev.*, 2019, **48**, 3181–3192.
35 T. Reier, M. Oezaslan and P. Strasser, *ACS Catal.*, 2012, **2**, 1765–1772.
36 L. Huo, B. Liu, G. Zhang, R. Si, J. Liu and J. Zhang, *J. Mater. Chem. A*, 2017, **5**, 4868–4878.
37 J. Li, M. Chen, D. A. Cullen, S. Hwang, M. Wang, B. Li, K. Liu, S. Karakalos, M. Lucero and H. Zhang, *Nat. Catal.*, 2018, **1**, 935–945.
38 C. Li, H. Liu and Z. Yu, *Appl. Catal., B*, 2019, **241**, 95–103.
39 C.-X. Zhao, J.-N. Liu, B.-Q. Li, D. Ren, X. Chen, J. Yu and Q. Zhang, *Adv. Funct. Mater.*, 2020, **30**, 2003619.
40 L. Wang, X. Wan, S. Liu, L. Xu and J. Shui, *J. Energy Chem.*, 2019, **39**, 77–87.
41 H. Wu, J. Wang, J. Yan, Z. Wu and W. Jin, *Nanoscale*, 2019, **11**, 20144–20150.
42 K. Im, D. Kim, J.-H. Jang, J. Kim and S. J. Yoo, *Appl. Catal., B*, 2020, **260**, 118192.
43 L. Liu, B. Wang, R. Gao, D. Zhang, W. Xu, L. Chen, X. Yan and Y. Li, *RSC Adv.*, 2020, **10**, 10689–10694.
44 E. Antolini, *Appl. Catal., B*, 2012, **123**, 52–68.
45 X. Zhou, J. Qiao, L. Yang and J. Zhang, *Adv. Energy Mater.*, 2014, **4**, 1301523.
46 S. H. Hur and J. N. Park, *Asia-Pac. J. Chem. Eng.*, 2013, **8**, 218–233.
47 M. Sharma, J.-H. Jang, D. Y. Shin, J. A. Kwon, D.-H. Lim, D. Choi, H. Sung, J. Jang, S.-Y. Lee, K. Y. Lee, H.-Y. Park, N. Jung and S. J. Yoo, *Energy Environ. Sci.*, 2019, **12**, 2200–2211.
48 H. Sung, M. Sharma, J. Jang, S.-Y. Lee, M.-G. Choi, K. Lee and N. Jung, *Nanoscale*, 2019, **11**, 5038–5047.
49 Y. Hu, Y. Lu, X. Zhao, T. Shen, T. Zhao, M. Gong, K. Chen, C. Lai, J. Zhang, H. L. Xin and D. Wang, *Nano Res.*, 2020, **13**, 2365–2370.
50 H.-J. Niu, L. Zhang, J.-J. Feng, Q.-L. Zhang, H. Huang and A.-J. Wang, *J. Colloid Interface Sci.*, 2019, **552**, 744–751.
51 D. Y. Chung, S. W. Jun, G. Yoon, S. G. Kwon, D. Y. Shin, P. Seo, J. M. Yoo, H. Shin, Y.-H. Chung, H. Kim, B. S. Mun, K.-S. Lee, N.-S. Lee, S. J. Yoo, D.-H. Lim, K. Kang, Y.-E. Sung and T. Hyeon, *J. Am. Chem. Soc.*, 2015, **137**, 15478–15485.
52 Z. Zhang, S. Liu, X. Tian, J. Wang, P. Xu, F. Xiao and S. Wang, *J. Mater. Chem. A*, 2017, **5**, 10876–10884.
53 J. Hwang, Y. Kim, M. Karuppnan, T. Lim and O. J. Kwon, *Electrocatalysis*, 2020, **11**, 77–85.
54 H. Ning, G. Li, Y. Chen, K. Zhang, Z. Gong, R. Nie, W. Hu and Q. Xia, *ACS Appl. Mater. Interfaces*, 2018, **11**, 1957–1968.
55 C. C. Yang, S. F. Zai, Y. T. Zhou, L. Du and Q. Jiang, *Adv. Funct. Mater.*, 2019, **29**, 1901949.
56 Y. Gao, H. Peng, Y. Wang, G. Wang, L. Xiao, J. Lu and L. Zhuang, *ACS Appl. Mater. Interfaces*, 2020, **12**, 31575–31581.
57 H. Fei, Y. Yang, Z. Peng, G. Ruan, Q. Zhong, L. Li, E. L. Samuel and J. M. Tour, *ACS Appl. Mater. Interfaces*, 2015, **7**, 8083–8087.
58 S. Li, W. Chen, H. Pan, Y. Cao, Z. Jiang, X. Tian, X. Hao, T. Maiyalagan and Z.-J. Jiang, *ACS Sustainable Chem. Eng.*, 2019, **7**, 8530–8541.
59 J. Deng, P. Ren, D. Deng, L. Yu, F. Yang and X. Bao, *Energy Environ. Sci.*, 2014, **7**, 1919–1923.
60 C. H. Choi, H. C. Kwon, S. Yook, H. Shin, H. Kim and M. Choi, *J. Phys. Chem. C*, 2014, **118**, 30063–30070.
61 Y. Shen, Y. Zhou, D. Wang, X. Wu, J. Li and J. Xi, *Adv. Energy Mater.*, 2018, **8**, 1701759.
62 C. Wang, H. Yang, Y. Zhang and Q. Wang, *Angew. Chem., Int. Ed.*, 2019, **58**, 6099–6103.
63 L. Du, L. Luo, Z. Feng, M. Engelhard, X. Xie, B. Han, J. Sun, J. Zhang, G. Yin and C. Wang, *Nano Energy*, 2017, **39**, 245–252.
64 H. Kim, A. W. Robertson, S. O. Kim, J. M. Kim and J. H. Warner, *ACS Nano*, 2015, **9**, 5947–5957.
65 X. Cui, P. Ren, D. Deng, J. Deng and X. Bao, *Energy Environ. Sci.*, 2016, **9**, 123–129.
66 M. Tavakkoli, T. Kallio, O. Reynaud, A. G. Nasibulin, C. Johans, J. Sainio, H. Jiang, E. I. Kauppinen and K. Laasonen, *Angew. Chem.*, 2015, **127**, 4618–4621.
67 R. S. Bhoria, in *Graphene and Its Derivatives-Synthesis and Applications*, IntechOpen, 2019.
68 J. Wang, J. Kim, S. Choi, H. Wang and J. Lim, *Small Methods*, 2020, **4**, 2000621.
69 C. Gao, F. Lyu and Y. Yin, *Chem. Rev.*, 2020, **121**, 934.
70 K. Hu, T. Ohto, L. Chen, J. Han, M. Wakisaka, Y. Nagata, J.-I. Fujita and Y. Ito, *ACS Energy Lett.*, 2018, **3**, 1539–1544.
71 H. Zhang, Z. Ma, J. Duan, H. Liu, G. Liu, T. Wang, K. Chang, M. Li, L. Shi and X. Meng, *ACS Nano*, 2016, **10**, 684–694.
72 Q. Hu, X. Liu, B. Zhu, L. Fan, X. Chai, Q. Zhang, J. Liu, C. He and Z. Lin, *Nano Energy*, 2018, **50**, 212–219.
73 Y. Zhang, Y. Ma, Y.-Y. Chen, L. Zhao, L.-B. Huang, H. Luo, W.-J. Jiang, X. Zhang, S. Niu and D. Gao, *ACS Appl. Mater. Interfaces*, 2017, **9**, 36857–36864.
74 D. Y. Chung, S. W. Jun, G. Yoon, H. Kim, J. M. Yoo, K.-S. Lee, T. Kim, H. Shin, A. K. Sinha and S. G. Kwon, *J. Am. Chem. Soc.*, 2017, **139**, 6669–6674.

This journal is © The Royal Society of Chemistry 2021

Published on 19 2564. Downloaded on 1/2/2569 7:34:44.

75 M. Karuppannan, J. E. Park, H. E. Bae, Y.-H. Cho and O. J. Kwon, *Nanoscale*, 2020, **12**, 2542–2554.
76 Y. Yang, Z. Lun, G. Xia, F. Zheng, M. He and Q. Chen, *Energy Environ. Sci.*, 2015, **8**, 3563–3571.
77 L. Li, B. Yan, L. Zhang, Y. Tian and H. Zeng, *Chem. Commun.*, 2015, **51**, 15780–15783.
78 Y. Kim, A. A. Jeffery, J. Min and N. Jung, *J. Nanomater.*, 2019, **9**, 1491.
79 J. Min, A. A. Jeffery, Y. Kim and N. Jung, *J. Nanomater.*, 2019, **9**, 1425.
80 J. Jang, M. Sharma, D. Choi, Y. S. Kang, Y. Kim, J. Min, H. Sung, N. Jung and S. J. Yoo, *ACS Appl. Mater. Interfaces*, 2019, **11**, 27735–27742.
81 J. Jang, M. Sharma, H. Sung, S. Kim and N. Jung, *Korean J. Mater. Res.*, 2018, **28**, 646–652.
82 H. Sung, M. Sharma, J. Jang and N. Jung, *Korean J. Mater. Res.*, 2018, **28**, 633–639.
83 M. Sharma, N. Jung and S. J. Yoo, *Chem. Mater.*, 2018, **30**, 2–24.
84 S.-F. Xue, W.-Y. Wu, X. Bian, Z.-F. Wang and Y.-F. Wu, *Green Process. Synth.*, 2018, **7**, 241–247.
85 C. Lv, B. Liang, K. Li, Y. Zhao and H. Sun, *Biosens. Bioelectron.*, 2018, **117**, 802–809.
86 J. Wang, D. Gao, G. Wang, S. Miao, H. Wu, J. Li and X. Bao, *J. Mater. Chem. A*, 2014, **2**, 20067–20074.
87 J. A. Varnell, C. Edmund, C. E. Schulz, T. T. Fister, R. T. Haasch, J. Timoshenko, A. I. Frenkel and A. A. Gewirth, *Nat. Commun.*, 2016, **7**, 1–9.
88 M. X. Chen, M. Zhu, M. Zuo, S. Q. Chu, J. Zhang, Y. Wu, H. W. Liang and X. Feng, *Angew. Chem., Int. Ed.*, 2020, **59**, 1627–1633.
89 R. Jasinski, *Nature*, 1964, **201**, 1212–1213.
90 Y. Xu, S. Yin, C. Li, K. Deng, H. Xue, X. Li, H. Wang and L. Wang, *J. Mater. Chem. A*, 2018, **6**, 1376–1381.
91 H. Liu, D.-H. Yang, X.-Y. Wang, J. Zhang and B.-H. Han, *J. Colloid Interface Sci.*, 2021, **581**, 362–373.
92 G. Zhang, W. Lu, F. Cao, Z. Xiao and X. Zheng, *J. Power Sources*, 2016, **302**, 114–125.
93 L. Zhang, C. Qi, A. Zhao, G. Xu, J. Xu, L. Zhang, C. Zhang and D. Jia, *Appl. Surf. Sci.*, 2018, **445**, 462–470.
94 Y. Xu, W. Tu, B. Zhang, S. Yin, Y. Huang, M. Kraft and R. Xu, *Adv. Mater.*, 2017, **29**, 1605957.
95 H. Lee, Y.-E. Sung, I. Choi, T. Lim and O. J. Kwon, *J. Power Sources*, 2017, **362**, 228–235.
96 S. Gong, C. Wang, P. Jiang, K. Yang, J. Lu, M. Huang, S. Chen, J. Wang and Q. Chen, *J. Mater. Chem. A*, 2019, **7**, 15079–15088.
97 X. Yan, C. L. Dong, Y. C. Huang, Y. Jia, L. Zhang, S. Shen, J. Chen and X. Yao, *Small Methods*, 2019, **3**, 1800439.
98 M. Gobbi, S. Bonacchi, J. X. Lian, Y. Liu, X.-Y. Wang, M.-A. Stoeckel, M. A. Squillaci, G. D'avino, A. Narita and K. Müllen, *Nat. Commun.*, 2017, **8**, 1–8.
99 J. Liu, W. Li, R. Cheng, Q. Wu, J. Zhao, D. He and S. Mu, *Langmuir*, 2019, **35**, 2580–2586.
100 Y. Xu, Y. Li, S. Yin, H. Yu, H. Xue, X. Li, H. Wang and L. Wang, *Nanotechnology*, 2018, **29**, 225403.
101 Y. He, Q. Tan, L. Lu, J. Sokolowski and G. Wu, *Electrochem. Energy Rev.*, 2019, **2**, 231–251.
102 X. Wang, Z. Li, Y. Qu, T. Yuan, W. Wang, Y. Wu and Y. Li, *Chem*, 2019, **5**, 1486–1511.
103 G. Giovannetti, P. A. Khomyakov, G. Brocks, V. V. Karpan, J. van den Brink and P. J. Kelly, *Phys. Rev. Lett.*, 2008, **101**, 026803.
104 F. Yang, D. Deng, X. Pan, Q. Fu and X. Bao, *Natl. Sci. Rev.*, 2015, **2**, 183–201.
105 D. Deng, K. Novoselov, Q. Fu, N. Zheng, Z. Tian and X. Bao, *Nat. Nanotechnol.*, 2016, **11**, 218–230.
106 Y. Peng and S. Chen, *Green Energy Environ.*, 2018, **3**, 335–351.
107 J. Deng, D. Deng and X. Bao, *Adv. Mater.*, 2017, **29**, 1606967.
108 W. Zhou, J. Jia, J. Lu, L. Yang, D. Hou, G. Li and S. Chen, *Nano Energy*, 2016, **28**, 29–43.
109 D. Deng, L. Yu, X. Chen, G. Wang, L. Jin, X. Pan, J. Deng, G. Sun and X. Bao, *Angew. Chem.*, 2013, **125**, 389–393.
110 L. Liang, J. Wang, W. Lin, B. G. Sumpter, V. Meunier and M. Pan, *Nano Lett.*, 2014, **14**, 6400–6406.
111 A. Castro-Neto and F. Guinea, *Rev. Mod. Phys.*, 2009, **81**, 109.
112 P. Geerlings, F. De Proft and W. Langenaeker, *Chem. Rev.*, 2003, **103**, 1793–1874.
113 J. Deng, P. Ren, D. Deng and X. Bao, *Angew. Chem., Int. Ed.*, 2015, **54**, 2100–2104.
114 J. Deng, L. Yu, D. Deng, X. Chen, F. Yang and X. Bao, *J. Mater. Chem. A*, 2013, **1**, 14868–14873.
115 M. Miao, R. Hou, Z. Liang, R. Qi, T. He, Y. Yan, K. Qi, H. Liu, G. Feng and B. Y. Xia, *J. Mater. Chem. A*, 2018, **6**, 24107–24113.
116 J. R. Kitchin, J. K. Nørskov, M. A. Barteau and J. Chen, *Phys. Rev. Lett.*, 2004, **93**, 156801.
117 J. Chen, G. Xia, P. Jiang, Y. Yang, R. Li, R. Shi, J. Su and Q. Chen, *ACS Appl. Mater. Interfaces*, 2016, **8**, 13378–13383.
118 A. F. Pedersen, E. T. Ulrikkeholm, M. Escudero-Escribano, T. P. Johansson, P. Malacrida, C. M. Pedersen, M. H. Hansen, K. D. Jensen, J. Rossmeisl and D. Friebel, *Nano Energy*, 2016, **29**, 249–260.
119 Y. Yang, Z. Lin, S. Gao, J. Su, Z. Lun, G. Xia, J. Chen, R. Zhang and Q. Chen, *ACS Catal.*, 2017, **7**, 469–479.
120 W. Zhou, T. Xiong, C. Shi, J. Zhou, K. Zhou, N. Zhu, L. Li, Z. Tang and S. Chen, *Angew. Chem., Int. Ed.*, 2016, **55**, 8416–8420.
121 A. Chen and C. Ostrom, *Chem. Rev.*, 2015, **115**, 11999–12044.
122 W. Ju, T. Brülle, M. Favaro, L. Perini, C. Durante, O. Schneider and U. Stimming, *ChemElectroChem*, 2015, **2**, 547–558.
123 S. Cherevko, A. R. Zeradjanin, A. A. Topalov, N. Kulyk, I. Katsounaros and K. J. Mayrhofer, *ChemCatChem*, 2014, **6**, 2219–2223.
124 S. Cherevko, S. Geiger, O. Kasian, N. Kulyk, J.-P. Grote, A. Savan, B. R. Shrestha, S. Merzlikin, B. Breitbach and A. Ludwig, *Catal. Today*, 2016, **262**, 170–180.

Published on 19 2564. Downloaded on 1/2/2569 7:34:44.

125 Q. Yin, J. M. Tan, C. Besson, Y. V. Geletii, D. G. Musaev, A. E. Kuznetsov, Z. Luo, K. I. Hardcastle and C. L. Hill, *Science*, 2010, **328**, 342–345.
126 G. C. Dismukes, R. Brimblecombe, G. A. Felton, R. S. Pryadun, J. E. Sheats, L. Spiccia and G. F. Swiegers, *Acc. Chem. Res.*, 2009, **42**, 1935–1943.
127 J. Wang, H. Wu, D. Gao, S. Miao, G. Wang and X. Bao, *Nano Energy*, 2015, **13**, 387–396.
128 X. Chen, J. Xiao, J. Wang, D. Deng, Y. Hu, J. Zhou, L. Yu, T. Heine, X. Pan and X. Bao, *Chem. Sci.*, 2015, **6**, 3262–3267.
129 B. J. Schultz, C. Jaye, P. S. Lysaght, D. A. Fischer, D. Prendergast and S. Banerjee, *Chem. Sci.*, 2013, **4**, 494–502.
130 X. Liu, T. Pichler, M. Knupfer and J. Fink, *Phys. Rev. B: Condens. Matter Mater. Phys.*, 2004, **70**, 245435.
131 Y. Feng, X.-Y. Yu and U. Paik, *Sci. Rep.*, 2016, **6**, 1–8.
132 J. Wang and F. Ciucci, *Small*, 2017, **13**, 1604103.
133 S.-W. Park, I. Kim, S.-I. Oh, J.-C. Kim and D.-W. Kim, *J. Catal.*, 2018, **366**, 266–274.
134 Y. Bing, H. Liu, L. Zhang, D. Ghosh and J. Zhang, *Chem. Soc. Rev.*, 2010, **39**, 2184–2202.
135 F. Hasché, M. Oezaslan and P. Strasser, *ChemCatChem*, 2011, **3**, 1805–1813.
136 P. Strasser, S. Koh, T. Anniyev, J. Greeley, K. More, C. Yu, Z. Liu, S. Kaya, D. Nordlund and H. Ogasawara, *Nat. Chem.*, 2010, **2**, 454–460.
137 K. Mohanraju and L. Cindrella, *RSC Adv.*, 2014, **4**, 11939–11947.
138 M. Oezaslan and P. Strasser, *J. Power Sources*, 2011, **196**, 5240–5249.
139 R. Sgarbi, K. Kumar, F. Jaouen, A. Zitolo, E. A. Ticianelli and F. Maillard, *J. Solid State Electrochem.*, 2019, 1–12.
140 M. M. Hossen, K. Artyushkova, P. Atanassov and A. Serov, *J. Power Sources*, 2018, **375**, 214–221.
141 P. G. Santori, F. D. Speck, S. Cherevko, H. A. Firouzjaie, X. Peng, W. E. Mustain and F. Jaouen, *J. Electrochem. Soc.*, 2020, **167**, 134505.
142 H. Kishi, T. Sakamoto, K. Asazawa, S. Yamaguchi, T. Kato, B. Zulevi, A. Serov, K. Artyushkova, P. Atanassov and D. Matsumura, *J. Nanomater.*, 2018, **8**, 965.
143 S. G. Peera, H. J. Kwon, T. G. Lee, J. Balamurugan and A. M. Hussain, *Novel Catalyst Materials for Bioelectrochemical Systems: Fundamentals and Applications*, 2020, pp. 231–278.
144 H. Lee, M. J. Kim, T. Lim, Y.-E. Sung, H.-J. Kim, H.-N. Lee, O. J. Kwon and Y.-H. Cho, *Sci. Rep.*, 2017, **7**, 1–8.
145 H.-C. Huang, Y.-C. Lin, S.-T. Chang, C.-C. Liu, K.-C. Wang, H.-P. Jhong, J.-F. Lee and C.-H. Wang, *J. Mater. Chem. A*, 2017, **5**, 19790–19799.
146 X. Zou, X. Huang, A. Goswami, R. Silva, B. R. Sathe, E. Mikmeková and T. Asefa, *Angew. Chem.*, 2014, **126**, 4461–4465.
147 C. Shuai, Z. Mo, X. Niu, Y. Du, Q. Gao, J. Liu, N. Liu and R. Guo, *Appl. Surf. Sci.*, 2020, **532**, 147381.
148 P. Wei, X. Sun, Q. Liang, X. Li, Z. He, X. Hu, J. Zhang, M. Wang, Q. Li and H. Yang, *ACS Appl. Mater. Interfaces*, 2020, **12**, 31503–31513.
149 C.-H. Liu, Y.-J. Tang, X.-L. Wang, W. Huang, S.-L. Li, L.-Z. Dong and Y.-Q. Lan, *J. Mater. Chem. A*, 2016, **4**, 18100–18106.
150 Z. Wang, S. Peng, Y. Hu, L. Li, T. Yan, G. Yang, D. Ji, M. Srinivasan, Z. Pan and S. Ramakrishna, *J. Mater. Chem. A*, 2017, **5**, 4949–4961.
151 Q. Zhang, M. Fu, G. Ning, Y. Sun, H. Wang, X. Fan, H. Lu, Y. Zhang and H. Wang, *J. Colloid Interface Sci.*, 2020, **580**, 794–802.
152 Y. Zhou, K. Neyerlin, T. S. Olson, S. Pylypenko, J. Bult, H. N. Dinh, T. Gennett, Z. Shao and R. O'Hayre, *Energy Environ. Sci.*, 2010, **3**, 1437–1446.
153 H. R. Colón-Mercado and B. N. Popov, *J. Power Sources*, 2006, **155**, 253–263.
154 S. Rudi, D. Teschner, V. Beermann, W. Hetaba, L. Gan, C. Cui, M. Gliech, R. Schlögl and P. Strasser, *ACS Catal.*, 2017, **7**, 6376–6384.
155 A. S. Haile, W. Yohannes and Y. S. Mekonnen, *RSC Adv.*, 2020, **10**, 27346–27356.
156 G. Wang, B. Huang, L. Xiao, Z. Ren, H. Chen, D. Wang, H. D. Abruña, J. Lu and L. Zhuang, *J. Am. Chem. Soc.*, 2014, **136**, 9643–9649.
157 M. Bele, P. Jovanovič, A. Pavlišič, B. Jozinović, M. Zorko, A. Rečnik, E. Chernyshova, S. Hočevar, N. Hodnik and M. Gaberšček, *Chem. Commun.*, 2014, **50**, 13124–13126.
158 T. P. Johansson, E. T. Ulrikkeholm, P. Hernandez-Fernandez, P. Malacrida, H. Hansen, A. Bandarenka, J. Nørskov, J. Rossmeisl, I. Stephens and I. Chorkendorff, *Top. Catal.*, 2014, **57**, 245–254.
159 V. R. Stamenkovic, B. S. Mun, M. Arenz, K. J. Mayrhofer, C. A. Lucas, G. Wang, P. N. Ross and N. M. Markovic, *Nat. Mater.*, 2007, **6**, 241–247.
160 J. Gao, M. Mao, P. Li, R. Liu, H. Song, K. Sun and S. Zhang, *ACS Appl. Mater. Interfaces*, 2020, **12**, 6298–6308.
161 C. Galeano, C. Baldizzone, H. Bongard, B. Spliethoff, C. Weidenthaler, J. C. Meier, K. J. Mayrhofer and F. Schüth, *Adv. Funct. Mater.*, 2014, **24**, 220–232.
162 M. Karuppannan, Y. Kim, S. Gok, E. Lee, J. Y. Hwang, J.-H. Jang, Y.-H. Cho, T. Lim, Y.-E. Sung and O. J. Kwon, *Energy Environ. Sci.*, 2019, **12**, 2820–2829.
163 K. Wang, R. Wang, H. Li, H. Wang, X. Mao, V. Linkov and S. Ji, *Int. J. Hydrogen Energy*, 2015, **40**, 3875–3882.
164 H. Jiang, Y. Yao, Y. Zhu, Y. Liu, Y. Su, X. Yang and C. Li, *ACS Appl. Mater. Interfaces*, 2015, **7**, 21511–21520.
165 L. Li, L. Song, H. Guo, W. Xia, C. Jiang, B. Gao, C. Wu, T. Wang and J. He, *Nanoscale*, 2019, **11**, 901–907.
166 M. Zeng, Y. Liu, F. Zhao, K. Nie, N. Han, X. Wang, W. Huang, X. Song, J. Zhong and Y. Li, *Adv. Funct. Mater.*, 2016, **26**, 4397–4404.
167 F. Aftab, H. Duran, K. Kirchhoff, M. Zaheer, B. Iqbal, M. Saleem and S. N. Arshad, *Welcome to ICONN-2019*, 2020, p. 35.

 This journal is © The Royal Society of Chemistry 2021

Published on 19 2564. Downloaded on 1/2/2569 7:34:44.

168 Y. Yan, B. Y. Xia, B. Zhao and X. Wang, *J. Mater. Chem. A*, 2016, **4**, 17587–17603.
169 J. Masa, W. Xia, I. Sinev, A. Zhao, Z. Sun, S. Grützke, P. Weide, M. Muhler and W. Schuhmann, *Angew. Chem., Int. Ed.*, 2014, **53**, 8508–8512.
170 T. Reier, M. Oezaslan, P. Strasser and A. Catal, *J. Phys. Chem. Lett.*, 2012, **3**, 399–404.
171 M. Li, T. Liu, L. Fan, X. Bo and L. Guo, *J. Alloys Compd.*, 2016, **686**, 467–478.
172 Y. Wu, J. Meng, Q. Li, C. Niu, X. Wang, W. Yang, W. Li and L. Mai, *Nano Res.*, 2017, **10**, 2364–2376.
173 L. Zhang, J. Xiao, H. Wang and M. Shao, *ACS Catal.*, 2017, **7**, 7855–7865.
174 J. Wang, W. Cui, Q. Liu, Z. Xing, A. M. Asiri and X. Sun, *Adv. Mater.*, 2016, **28**, 215–230.
175 X. Zhang, H. Xu, X. Li, Y. Li, T. Yang and Y. Liang, *ACS Catal.*, 2016, **6**, 580–588.
176 H. Khani, N. S. Grundish, D. O. Wipf and J. B. Goodenough, *Adv. Energy Mater.*, 2020, **10**, 1903215.
177 N. Li, H. Tan, X. Ding, H. Duan, W. Hu, G. Li, Q. Ji, Y. Lu, Y. Wang and F. Hu, *Appl. Catal., B*, 2020, **266**, 118621.
178 B. K. Barman and K. K. Nanda, *ACS Sustainable Chem. Eng.*, 2018, **6**, 12736–12745.
179 S. H. Noh, M. H. Seo, J. Kang, T. Okajima, B. Han and T. Ohsaka, *NPG Asia Mater.*, 2016, **8**, e312–e312.
180 M. Wang, C. Zhang, T. Meng, Z. Pu, H. Jin, D. He, J. Zhang and S. Mu, *J. Power Sources*, 2019, **413**, 367–375.
181 Y. B. Adegbemiga, N. Ullah, M. Xie, S. Hussain, C. J. Oluigbo, W. Yaseen, A. J. Kumar, Y. Xu and J. Xie, *J. Alloys Compd.*, 2020, **835**, 155267.
182 M. R. Liu, Q. L. Hong, Q. H. Li, Y. Du, H. X. Zhang, S. Chen, T. Zhou and J. Zhang, *Adv. Funct. Mater.*, 2018, **28**, 1801136.
183 L. Yu, B. Y. Xia, X. Wang and X. W. Lou, *Adv. Mater.*, 2016, **28**, 92–97.
184 W. F. Chen, K. Sasaki, C. Ma, A. I. Frenkel, N. Marinkovic, J. T. Muckerman, Y. Zhu and R. R. Adzic, *Angew. Chem., Int. Ed.*, 2012, **51**, 6131–6135.
185 Z.-Y. Yu, Y. Duan, M.-R. Gao, C.-C. Lang, Y.-R. Zheng and S.-H. Yu, *Chem. Sci.*, 2017, **8**, 968–973.
186 X. Long, J. Li, S. Xiao, K. Yan, Z. Wang, H. Chen and S. Yang, *Angew. Chem.*, 2014, **126**, 7714–7718.
187 W. Ren, W. Zang, H. Zhang, J. Bian, Z. Chen, C. Guan and C. Cheng, *Carbon*, 2019, **142**, 206–216.
188 L. Shen, T. Sun, O. Zhuo, R. Che, D. Li, Y. Ji, Y. Bu, Q. Wu, L. Yang and Q. Chen, *ACS Appl. Mater. Interfaces*, 2016, **8**, 16664–16669.
189 Q. Wang, F. Chen, Y. Liu, T. T. Gebremariam, J. Wang, L. An and R. L. Johnston, *J. Power Sources*, 2018, **404**, 106–117.
190 G.-L. Li, B.-B. Yang, X.-C. Xu, S. Cao, Y. Shi, Y. Yan, X. Song and C. Hao, *Chem. – Eur. J.*, 2020, **26**, 2890–2896.
191 N. Wu, Y. Lei, Q. Wang, B. Wang, C. Han and Y. Wang, *Nano Res.*, 2017, **10**, 2332–2343.
192 X. Lv, J. Ren, Y. Wang, Y. Liu and Z.-Y. Yuan, *ACS Sustainable Chem. Eng.*, 2019, **7**, 8993–9001.
193 M. A. Ahsan, A. R. P. Santiago, M. F. Sanad and J. M. Weller, *J. Colloid Interface Sci.*, 2021, **581**, 905–918.
194 M. Khalid, A. M. B. Honorato, G. T. Filho and H. Varela, *J. Mater. Chem. A*, 2020, **8**, 9021–9031.
195 H. Guo, N. Youliwasi, L. Zhao, Y. Chai and C. Liu, *Appl. Surf. Sci.*, 2018, **435**, 237–246.
196 P. Jiang, J. Chen, C. Wang, K. Yang, S. Gong, S. Liu, Z. Lin, M. Li, G. Xia, Y. Yang, J. Su and Q. Chen, *Adv. Mater.*, 2018, **30**, 1705324.
197 J. Su, Y. Yang, G. Xia, J. Chen, P. Jiang and Q. Chen, *Nat. Commun.*, 2017, **8**, 14969.
198 F. Aftab, H. Duran, K. Kirchhoff, M. Zaheer, B. Iqbal, M. Saleem and S. N. Arshad, *ChemCatChem*, 2020, **12**, 932–943.
199 J. Yu, Y. Zhong, W. Zhou and Z. Shao, *J. Power Sources*, 2017, **338**, 26–33.
200 B. Du, Q.-T. Meng, J.-Q. Sha and J.-S. Li, *New J. Chem.*, 2018, **42**, 3409–3414.
201 S. Saha and A. K. Ganguli, *ChemistrySelect*, 2017, **2**, 1630–1636.
202 L. Yang, D. Wang, Y. Lv and D. Cao, *Carbon*, 2019, **144**, 8–14.
203 G. Zhong, S. Li, S. Xu, W. Liao, X. Fu and F. Peng, *ACS Sustainable Chem. Eng.*, 2018, **6**, 15108–15118.
204 B. Wang, Y. Ye, L. Xu, Y. Quan, W. Wei, W. Zhu, H. Li and J. Xia, *Adv. Funct. Mater.*, 2020, 2005834.
205 T. Li, Y. Lu, S. Zhao, Z.-D. Gao and Y.-Y. Song, *J. Mater. Chem. A*, 2018, **6**, 3730.